North Carolina Agricultural and Technical State University

Aggie Digital Collections and Scholarship

2014

Design Of Feedback Control For Active Mass Dampers Of Excited Structures

Sara Leona Bowen
North Carolina Agricultural and Technical State University

Follow this and additional works at: https://digital.library.ncat.edu/theses

Design of Feedback Control for Active Mass Dampers of Excited Structures

Sara Leona Bowen

North Carolina A&T State University

A thesis submitted to the graduate faculty

in partial fulfillment of the requirements for the degree of

MASTER OF SCIENCE

Department: Mechanical Engineering

Major: Mechanical Engineering

Major Professor: Dr. Sun Yi

Greensboro, North Carolina

2014

The Graduate School
North Carolina Agricultural and Technical State University

This is to certify that the Master's Thesis of

Sara Leona Bowen

has met the thesis requirements of
North Carolina Agricultural and Technical State University

Greensboro, North Carolina
2014

Approved by:

Dr. Sun Yi

Major Professor

Dr. Mannur Sundaresan

Committee Member

Dr. Miguel Picornell-Darder

Committee Member

Dr. Samuel Owusu-Ofori

Department Chairperson

Dr. Sanjiv Sarin

Dean, The Graduate School

BIOGRAPHICAL SKETCH

Sara Leona Bowen was born December 5, 1989, in Greensboro, North Carolina. She received a Bachelor of Science degree in Applied Mathematics and a minor in Physics from the University of North Carolina Wilmington in 2012. Currently, she is a candidate for a Master of Science degree in Mechanical Engineering at NC A&T State University.

DEDICATION

I dedicate this Master's Thesis to God, who has been my provider and guidance throughout my entire educational career. I also dedicate this work to my family and closest friends. Without their love, support and motivational words, I would not have been able to grow into the successful, educated woman that I am today.

ACKNOWLEDGMENTS

I acknowledge and express great gratitude toward the highly acclaimed Dr. Sun Yi for his professional guidance and support throughout my graduate studies at North Carolina A&T State University.

TABLE OF CONTENTS

LIST OF FIGURES

LIST OF TABLES

ABBREVIATIONS

AMD-1	Active Mass Damper - One Floor
AR	Auto-regressive
AWS	Active Wireless Sensing
DOF	Degree(s)-Of-Freedom
EMF	ElectroMotive-Force
EOM	Equation of Motion
FB	Feedback
FF	Feedforward
LSS	Large Space Structures
LQR	Linear Quadratic Regulation
MDS	Mass Damper System
MIMO	Multi-Input and Multi-Output
MPC	Model Predictive Control
PEA	Partial Eigenvalue Analysis
PID	Proportional-Integrated-Derivative
PV	Proportional-Velocity
RMS	Root Mean Square
SDS	Supplementary Damping Systems
SISO	Single-Input and Single-Output
TLCD	Tuned Liquid Column Damper
TMD	Tuned Mass Damper
TSD	Tuned Sloshing Damper
Y-W	Yule-Walker

PHYSICAL CONSTANTS

Constant Name	Symbol	=	Value (with units)
Amplifier Maximum Output Current	$IMAX_{AMP}$	=	4 A
Amplifier Maximum Output Voltage	$VMAX_{AMP}$	=	24 V
Cart Back-EMF Constant	K_m	=	.0077 Vs/rad
Cart Equivalent Viscous Damping Coefficient, as seen at the Motor Pinion	B_{eq}	=	3
Cart Mass	M_c	=	.65 kg
Cart Motor Armature Resistance	R_m	=	2.6 Ohm
Cart Motor Armature Voltage	V_m	=	.8 V
Cart Motor Efficiency	η_m	=	1
Cart Rotor Inertia	J_m	=	3.9×10^{-7} kgm^2
Cart Motor Pinion Radius	r_{mp}	=	.064 m
Cart Motor Torque Constant	K_t	=	.0077 Nm/A
Cart Planetary Gearbox Efficiency	η_g	=	1
Cart Planetary Gearbox Gear Ratio	K_g	=	3.71
Floor Accelerometer Sensitivity	K_{ACC}	=	9.81 m/s^2/V

Initial Approximations:

Structure Viscous Damping Coefficient	B_f	=	0 Ns/m
Floor Mass	M_f	=	1.38 kg
Floor Stiffness	K_f	=	500.9 N/m

SYMBOLS

Symbol	MATLAB	Description	Unit
J		Cost Function	
L		Lagrangian	J
M_p		Percent Overshoot	%
Q_{xc}		Generalized Force,	N
		Applied on the Generalized Coordinate x_c	
Q_{xf}		Generalized Force,	N
		Applied on the Generalized Coordinate x_f	
s		Laplace Operator	
t_p		Peak Time	s
t_s		Settling Time	s
Tt_c		Cart Translational Kinetic Energy	J
Tr_c		Cart Rotor Rotational Kinetic Energy	J
Tt_f		Floor Translational Kinetic Energy	J
T_T		Total Kinetic Energy of the AMD-1 System	J
V_T		Total Potential Energy of the AMD-1 System	J
A	A	System Matrix	
B	B	Input Matrix	
C	C	Output Matrix	
CO	CO	Controllability Matrix	
D	D	Input-Output Matrix	
G	G	Full-Order State Observer Gain Matrix	
K	K	Full-State Feedback Gain Vector	
OP	OP	Closed-Loop Pole Vector,	

		due to the Observer Error Dynamics	
P	P	Closed-Loop Pole Vector,	
		due to the State Feedback Law	
W	W	Observability Matrix	
X	X	Actual State Vector	
X₀	X0	Estimated State Vector	
Y	Y	Actual Output Vector	
Y₀	Y0	Estimated Output Vector	

B_f	Bf	Structure Viscous Damping Coefficient	Ns/m
B_{eq}	Beq	Cart Equivalent Viscous Damping Coefficient,	
		as seen at the Motor Pinion	
F_c	Fc	Cart Driving Force (produced by the DC motor)	N
$IMAX_{AMP}$	IMAX_AMP	Amplifier Maximum Output Current	A
K_{ACC}	K_ACC	Floor Accelerometer Sensitivity	$m/s^2/V$
K_f	Kf	Floor Stiffness	N/m
K_g	Kg	Cart Planetary Gearbox Gear Ratio	
K_m	Km	Cart Back-EMF Constant	V
K_t	Kt	Cart Motor Torque Constant	Nm
J_m	Jm	Cart Rotor Inertia	kgm^2
M_c	Mc	Cart Mass	kg
M_f	Mf	Floor Mass	kg
η_g	Eff_g	Cart Planetary Gearbox Efficiency	
η_m	Eff_m	Cart Motor Efficiency	
R_m	Rm	Cart Motor Resistance	Ohm
r_{mp}	r_mp	Cart Motor Pinion Radius	mm
V_m	Vm	Cart Motor Voltage	V

$VMAX_{AMP}$	VMAX_AMP	Amplifier Maximum Output Voltage	V
x_c	xc	Cart Position	m
$\dot{x}_c$	xc_dot	Cart Velocity	m/s
$\ddot{x}_c$	xc_ddot	Cart Acceleration	m/s^2
x_f	xf	Floor Position	m
$\dot{x}_f$	xf_dot	Floor Velocity	m/s
$\ddot{x}_f$	xf_ddot	Floor Acceleration	m/s^2

ABSTRACT

Annually, our world experiences thousands of seismic events that are the cause of hundreds of structural disasters and human fatalities. The objective of the presented research is to contribute to the world's social, economic, and environmental needs by designing an optimized feedback control for active mass dampers (AMDs) by reducing oscillations. The optimal design will meet the required specifications and maintain a structure's quasi-ideal, static position throughout a seismic event. The system's equation of motion (EOM) is derived by using the Lagrangian Method and the free-body diagram. All the simulated and experimental responses of the AMD-1 system are obtained using MATLAB and Simulink. The experimental data is collected from various tests performed on a single-story building model. The techniques utilized for improvement of the AMD's feedback control include parameter estimation, eigenvalue assignment, and linear quadratic regulation (LQR). As success is achieved with the AMD feedback control, future research can focus on idealizing the AMD's performance in a system with multiple degrees of freedom.

CHAPTER 1

INTRODUCTION

1.1   Motivation

Annually, our world experiences thousands of natural disasters (seismic events) that are the cause of hundreds of structural disasters and human fatalities. These disasters can be the effect of high wind speeds or an excitation of the Earth's crust. A map of the global economic effect of leading natural disasters, since 1980, is portrayed in Figure 1.1 [22]. This map recognizes China, Japan, United States, Thailand, Chile and the Caribbean Islands as the primary world victims of natural disasters, and they are ranked in the order of most to least number of casualties. The summed number of deaths, caused by each natural disaster, and their percentages are organized into Table 1.1, where it clearly shows that earthquakes are the leading cause of the world's natural disaster related deaths.

FIGURE 1.1: Leading natural disasters by overall economic loss and human fatality, since 1980 [22].

With respect to structural disasters, earthquakes have a growing negative impact on nuclear power plants. Figure 1.2 illustrates the worldwide location of both active earthquake

zones, based on the seismic data gathered from the United States Geological Survey, and nuclear power plants, based on the nuclear power station information gathered from the International Atomic Energy Agency [1, 26, 27]. The number of plants and the overall percentages of the top five countries, home to the most amount of nuclear power plants in the world, are listed in Table 1.2. It is observed that two of the top three natural disaster victims (United States and Japan) are collectively home to over 35% of the world's nuclear power plants. This leads to a higher potential risk for social, economic, and environmental loss, particularly, but not limited to, the United States and Japanese areas.
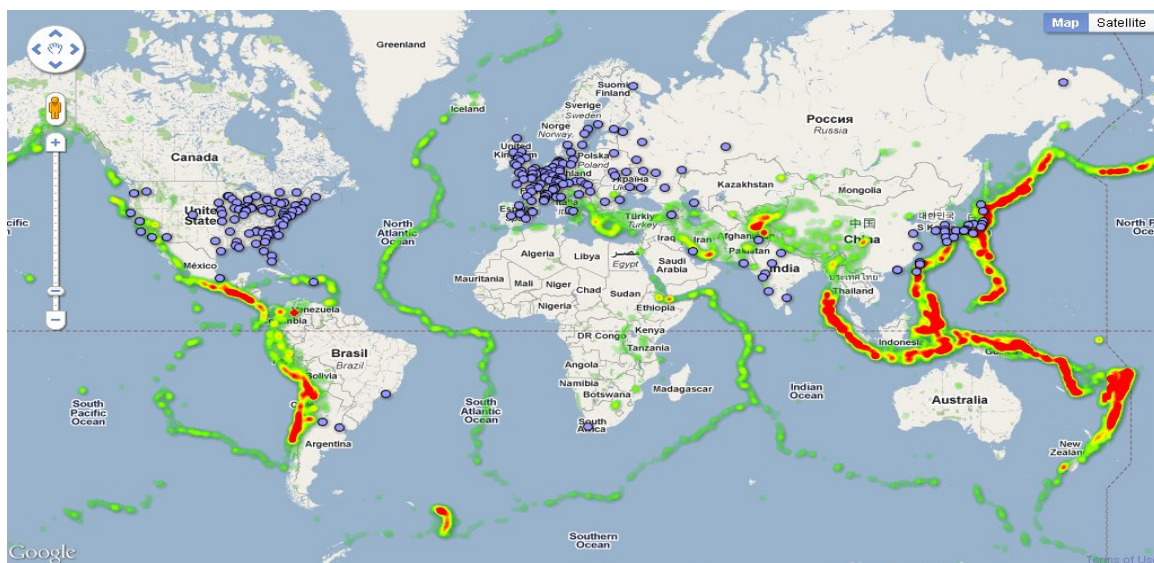
FIGURE 1.2: Global heat-map of active earthquake zones (green, yellow, red zones) and nuclear power plant locations (purple dots) [26].

TABLE 1.1: Leading Natural Disaster Deaths, Since 1980 [22]

Earth	**Water**	**Wind**
Earthquakes	Tsunamis & Floods	Hurricanes
106,897	22,654	1,492
81.57 %	17.29 %	1.14 %

TABLE 1.2: Countries with the Most Nuclear Power Plant Locations [1, 26, 27]

Country	Plants	Worldly %
United States	79	31.73 %
Germany	26	10.44 %
France	22	8.84 %
Japan	19	7.63 %
United Kingdom	17	6.83 %
Total Plants	249	65.47 %

1.2 Solution and Concerns

A potential solution to this problem includes the installation of active mass dampers (AMDs) into the buildings and plants at risk. In the 1980's, researchers began considering the use of AMDs to achieve structural control [38]. Yet in 2011, thirty years later, it was still rare to hear about any such installations [32]. This hesitation, to commercially utilize AMDs, could have been the result of several different limitations and concerns. When modeling large space structures (LSS), the dynamics of the AMD system are nonlinear, and non-linearity can lead to mathematical complexity and uncertainty. Unfortunately, the AWS (active wireless sensing) units, used in wireless AMDs, have limited computational abilities that stem from the limited availability of voltage, money, and resources. Consider the design of feedback controllers in a MIMO (multi-input and multi-output) system, they require a vast amount of input voltage, resulting in extremely high expenses. For this reason, restrictions must be put on the design of the feedback control. These design specifications are made to decrease the effect of these complications and lead to the design of a light weight device with a low power demand, a low energy consumption rate, and the utilization a robust control scheme [3, 13, 32, 33, 38].

1.3 Application

The development and implementation of the feedback control design specifications lead to an increased usage of AMDs. As of last year (2013), AMDs had been installed in fifty Japanese buildings, one of which was a twenty four-story building in Tokyo, which survived the 2011 typhoon and earthquake. The AMD's performance was closely monitored, and the results suggested the AMD's control performance and energy regeneration efforts were successful. Analysis of this data provided evidence that the regeneration system saved as much as 35-65% of the energy that the AMD was predicted to have consumed without it. Verification of this success is presented in [39].

The objective of the presented research is to further contribute to the World's social, economic, and environmental needs by designing an ideal feedback control for AMDs. It is intended that the optimized design will meet the required specifications and maintain a structure's quasi-ideal, static position throughout a seismic event. The system used in this work is a one story building model with an installed AMD (AMD-1). To design the feedback control, the system's equation of motion (EOM) is derived by using the Lagrangian Method and the free body diagram. Simulated and experimental AMD-1 responses are obtained from a variety of tests using MATLAB and Simulink. The techniques used for improvement of the AMD's feedback control include parameter estimation, eigenvalue assignment, and linear quadratic regulation (LQR). As success is achieved with the AMD feedback control, future research can focus on idealizing the AMD's performance in a MIMO system.

CHAPTER 2

LITERATURE REVIEW

Exceptional progress has been made in the field of system dynamics with respect to structural control. Structural design techniques have evolved over the years to help structures withstand seismic events and ensure safety to those in and around the structure. The use of various supplementary damping systems (SDS) and mass damping systems (MDS) have been widely studied and tested on structures susceptible to seismic excitation. Within these damping systems, lies a controller that is used to increase the decay rate of the system. Depending on the characteristics of the system-to-be-controlled, these controllers have the potential to be highly complex and demand an intricate design. This section provides a brief background and description for a variety of damping systems and controller design techniques.

2.1   Supplementary Damping Systems

A Supplementary Damping System (SDS) is a control system that is designed to absorb structure vibrations [30]. Three of the main types of SDS are passive, semi-active, and active control systems. Passive control is the simplest and cheapest form of an SDS. This type of system uses mechanical control forces to oppose the motion of the structure, and requires no external power. Consequently, its performance is always reliable, even in the event of a power outage. The downfall is, a passive system is unable to adapt to the fluctuation of the system's parameters (mass, damping coefficient and stiffness) over time.

In a semi-active SDS, the system's parameters can be modified to update the control system. Control is achieved by counteracting the structure's motion with controlled resistive forces, which requires a small amount of external power. Since the system utilizes the structure's motion to develop these control forces, stability is always guaranteed; however, the

performance is limited. It achieves the highest efficiency in situations where the dynamic characteristics and excitation conditions are well known.

Active control systems are the more modern form of control systems and are found to be the most versatile. They possess the ability to both add and dissipate energy in the system by the use of force generators. These generators have a high demand for power, which can lead to high expenses, and if the system were to go into an out-of-control state, it can increase the potential for system destabilization [17, 30]. Despite these concerns, an active control system was chosen to be used in this study because it has the highest potential for increased success.

2.2   Mass Damping Systems

Mass damper systems (MDS) are specific types of SDSs that use the the weight of a mass to dissipate the energy transferred to the structure by a seismic event. The most effective location for such systems is at or near the area where the vibration is at the highest amplitude. Typically, this is at the top or bottom of a structure, or at the outermost point of an overhang. The four most popular types of dampers used in these systems are tuned liquid column dampers, tuned sloshing dampers, tuned mass dampers, and active mass dampers [30].

Tuned liquid column dampers (TLCD) are one of the cheapest in cost. They use the mass and motion of a liquid, stored in a U-shaped tank, to counteract the vibration of a structure. Further energy dissipation can be achieved simply by installing adjustable gates. The Bernoulli's equation is used to derive this system's dynamics, and is shown to only achieve effectiveness in one axis [11].

Tuned sloshing dampers (TSD) use the surface waves of a liquid to absorb a structure's vibration. The tank, used to hold the liquid, is specifically engineered so that the frequency of the liquid's surface wave matches the natural frequency of the structure. Similar to the TLCD, the tank also incorporates baffles to further dissipate energy, but effectiveness can be achieved in two orthogonal axes, simultaneously, when a rectangular tank is used [30].

Tuned Mass Dampers (TMD) use a mass (typically steel or concrete) suspended on cables to counteract the force on a structure. In situations were minimum height requirements become a variable in the problem, two masses, suspended by a combination of cables and struts, are used. TMDs are tuned to be effective in two axes, simultaneously, and they incorporate hydraulic cylinders to dissipate energy [20, 30].

Active Mass Dampers (AMD) are similar to TMDs, but they stabilize the system by utilizing a driving mechanism instead of energy dissipators. Typically hydraulic actuators, with their high durability and high cost performance rating, are used to drive the system, and are based on the structure's motion sensor input. The driving mechanism is controlled by a computer, and therefore requires power, but it allows the control system to react to the structure's motion in real time [38]. It is For this reason that an AMD was chosen to be used in this study.

2.3   Controller Design

Within the AMD of this study's active control system, there exists a controller. The design of this controller must be unique to the provided system. Research suggests that the most popular controller design methods include the eigenvalue assignment method and linear quadratic regulator (LQR) design. Some newer controller design methods that have been utilized in other studies include model predictive control (MPC) and adaptive control. It was decided that the newness of these control methods imply there is still much to be learned about them and they lack in reliability. For that reason, only the eigenvalue assignment method and LQR design will be used in this study. Nonetheless, a brief background and description for each of these controller design techniques is provided in this section for enlightening purposes.

2.3.1   Eigenvalue Assignment

To utilize the eigenvalue assignment method, the system must be written in the state-space form shown in equation (2.1).

$$\dot{\mathbf{x}} = \mathbf{A}\mathbf{x} + \mathbf{B}u \tag{2.1a}$$

$$\mathbf{y} = \mathbf{C}\mathbf{x} + \mathbf{D}u \tag{2.1b}$$

Vector $\mathbf{x}$ is defined as the state vector and $\dot{\mathbf{x}}$ is the derivative of the state vector. These two vectors are used to represent all the measurable variables in the system (position, velocity, and acceleration). In a real life situation, it is not always possible, or necessary, to measure all these states; therefore, desired outputs are chosen from these states and represented by vector $\mathbf{y}$. The system input is represented by u, which is typically some kind of physical force or voltage. The relation between the states, inputs and outputs is represented by the state-space matrices $\mathbf{A}$, $\mathbf{B}$, $\mathbf{C}$ and $\mathbf{D}$. The system matrix, $\mathbf{A}$, represents the relation between each of the states. The input matrix, $\mathbf{B}$, represents the relation between each state and the input. The output matrix, $\mathbf{C}$, represents the relation between the output(s) and states. Lastly, the input-output matrix, $\mathbf{D}$, is used to represent the relation between the input and the output(s).

The objective of eigenvalue assignment (aka: pole placement design) is to design a state-feedback gain vector, $\mathbf{K}$, that will control a system based on its open-loop eigenvalues (aka: poles or roots) and its desired time-domain specifications [3]. The open-loop eigenvalues are determined from the system's characteristic equation, denoted by: $\det(s\mathbf{I} - \mathbf{A}) = 0$, where $\mathbf{I}$ is the identity matrix and s is the Laplace operator. The time-domain specifications of the current system are defined by the output response's percent overshoot, M_p, settling time, t_s, and peak time, t_p. These values are determined from the system's damping coefficient, ζ, and

natural frequency, ω_n, found in the characteristic equation of standard second-order system:

$$s^2 + 2\zeta\omega_n s + \omega_n^2 = 0 \tag{2.2}$$

Based on the control theory, a system is only considered to be stable when all of its poles have negative real parts. In other words, they are all located to the left of the stability boundary, when plotted in the complex plane. This plot of the pole's location also indicates whether the system meets the desired specifications or not. If improvement it needed, the control theory also states that, stability, a reduction in the system's dynamic response, or a satisfaction of the time-domain specifications can be achieved by moving the location of the dominant closed-loop poles further to the left in the complex plane. This negative movement of the poles location increases the system's damping coefficient, and in turn decreases M_p, t_s, and t_p, which will be further discussed in the results section.

Recall, each pole of a differential equation contributes an exponential function to the power of "*at*" or "*rt*" to the system, where *a* represents the real part of an imaginary pole and *r* represents a real pole. The dominant pole is defined by the pole that produces the exponential function with the slowest decay rate (approaches zero last), because it has the most influence on the system response. In matrix form, a vector **K** is added to the system, to produce the stabilized or improved system shown in (2.3), where the closed-loop eigenvalues are found by satisfying: $\det(s\mathbf{I} - (\mathbf{A} - \mathbf{BK})) = 0$

$$\dot{\mathbf{x}} = (\mathbf{A} - \mathbf{BK})\mathbf{x} + \mathbf{B}u \tag{2.3a}$$

$$\mathbf{y} = \mathbf{Cx} + \mathbf{D}u \tag{2.3b}$$

Since this world is imperfect, moving the poles too far to the left will cause discrepancies. For this reason, it is important to determine and understand the limitations unique to each system. For example, active control has the potential to introduce time delays in the control effort's FB loop, and a MIMO system has a higher risk of asymptotic stability when using low-gain controllers [2, 3, 5, 8, 9, 12, 28, 34].

Some of the newest background on the eigenvalue assignment method includes the addressing of the issue regarding the degrading performance in controllers, for systems with time variant parameters, in 2007. This solution involved the utilization of eigenvalue assignment techniques to stabilize the system with both, robust and adaptive controllers. It was found that the robust pole placement controllers required lower actuator voltages than the adaptive pole placement controllers. But it was also found that the adaptive controllers were found to be noise tolerant, while the robust controllers were found to be noise sensitive. Furthermore, studies show that robust stability and performance can only be achieved for a select range of parameter uncertainties [14].

More recently, in 2011, a modified version of the eigenvalue assignment method was discussed, and referred to as partial eigenvalue analysis (PEA). In PEA, only a selection of the open-loop eigenvalues are modified in the FB controller. PEA was found to be effective because it can keep a structure safely active under excitation, with minimal control effort [4, 8].

2.3.2 Linear Quadratic Regulator

In 2005, three numerical design techniques, used for optimizing active structural control during seismic activity, were presented. These techniques include LQR, discrete time-dependent non-integral LQR, and generalized LQR. Reseach suggests that When designing an LQR system, it should be taken into consideration that they require multiple sensors, integrating amplifiers and cables to achieve vibration control. However, it is also suggested that by utilizing vibration control techniques that apply the robust control theory, the required equipment may be minimized [36]. Nonetheless, this issue was not presented in the work of this

thesis.

The objective of the LQR method is to obtain a control force, $u : [0, T] \to R^m$, that is proportional to the structural response and that minimizes the cost function, J [25]. This is achieved by utilizing an integral performance index and selecting the appropriate feedback gains and full-state observers, based on the input and output weight matrices [5, 10, 19, 35].

The cost function, for a continuous time system, is expressed by equation (2.4), where $\mathbf{R}$ represents the input weight matrix and $\mathbf{Q}$ represents the output weight matrix.

$$J(u) = \int_0^\infty \left(\mathbf{x}^T \mathbf{Q} \mathbf{x} + u^T \mathbf{R} u \right) dt \tag{2.4}$$

Given the system dynamics are described by equation (2.5), where $\mathbf{x}$ is the state vector, $\dot{\mathbf{x}}$ is the derivative of the state vector, $\mathbf{A}$ is the system matrix, and $\mathbf{B}$ is the input matrix.

$$\dot{\mathbf{x}} = \mathbf{A}\mathbf{x} + \mathbf{B}u \tag{2.5}$$

$\mathbf{J}$ gets minimized by the state feedback law, $u = -\mathbf{k}\mathbf{x}$. The minimized function returns the solution, $\mathbf{S}$, of the Riccati equation (2.6), and the closed loop poles, the determinant of $(\mathbf{A} - \mathbf{B}\mathbf{K})$ [5, 25].

$$\mathbf{A}^T \mathbf{S} + \mathbf{S}\mathbf{A} - \mathbf{S}\mathbf{B}\mathbf{R}^{-1}\mathbf{B}^T \mathbf{S} + \mathbf{Q} = 0 \tag{2.6}$$

Finally, the feedback gain vector, $\mathbf{K}$, is derived from $\mathbf{S}$ by the use of the following expression:

$$\mathbf{K} = \mathbf{R}^{-1}\mathbf{B}^T \mathbf{S} \tag{2.7}$$

The limitations of the LQR method include [25]:

- $(\mathbf{A}, \mathbf{B})$ must be stabilizable.
- $\mathbf{R} > 0$ and definite.

- $\mathbf{Q} \geq 0$ and semi-definite.

- $(\mathbf{Q}, \mathbf{A})$ must have no unobservable mode on the imaginary axis.

The discrete time-dependent non-integral LQR method is exactly the same as the LQR method, but it is for a discrete-time state-space model. The discrete feedback control law, $u[n] = \breve{}Kx[n]$, minimizes the discrete cost function (2.8), given the system dynamics (2.9). Since it is discrete, this method must reach optimality at every time instant and is used when the control forces are set to be proportional to both, the structural response and the time step [19, 25].

$$J = \sum_{n=0}^{\infty} \{\mathbf{x}^T \mathbf{Q} \mathbf{x} + u^T \mathbf{R} u\} \tag{2.8}$$

$$\mathbf{x}[n+1] = \mathbf{A}\mathbf{x}[n] + \mathbf{B}u[n] \tag{2.9}$$

Lastly, the generalized LQR, is simply defined as a generalization of the criteria from both the LQR and the discrete time-dependent non-integral LQR [19].

2.3.3 Model Predictive Control

In 2001, a general formulation of the (MPC) scheme was introduced by Mei and *et al.* The objective is to minimize both the trajectory deviation between the predicted and desired responses as well as the control effort subjected to specific constraints. This is achieved by using a prediction model of the system response, formulated using both feedforward (FF) and feedback (FB) loops, to control the real-time response of a seismically excited structure. [23].

To obtain the FF loop, two types of inputs were used: the Kanai-Tajimi Type model and an Auto-Regressive (AR) model. The Kanai-Tajimi model simulates an earthquake input based on the concept of a random pulse train. It also possesses the potential to incorporate the

propagation, reflection, and refraction of seismic waves as they travel through the ground [16]. The Auto-Regressive model simulates the ground motion of an earthquake with a real-time FF loop. It is constantly updated with real-time, on-line observations, which guarantees that control actions of the system will be able to compensate for the unusual ground behavior by employing both predictive and adaptive methods, despite time delays [23].

A year later, Mei and *et al.* formulated the prediction model with an acceleration FB loop that records acceleration measurements from a variety of locations on the structure. From the acceleration FB, the state observer estimates the system's state variables with the Kalman-Bucy filter. The effectiveness of the MPC scheme with the acceleration FB was validated from the experimental results of an AMD used on both a single and a three story building model. The results indicated that the MPC scheme, with the acceleration FB, performed just as good or better than it did with the state FB [24].

In 2008, a numerical computation method for optimizing a control action, that took the MPC scheme limitations into consideration, was devised [37]. Similar techniques had been used in other fields of study; however, the high computational requirements of the MPC, restricts its use to systems with slow dynamics. furthermore, it was concluded that, with the basic online quadratic programming methods, the MPC showed compelling control performance when used at high sampling rates on inexpensive hardware [37].

2.3.4 *Adaptive Control*

Adaptive controllers maintain ideal performance under fluctuating conditions by incorporating a mechanism that estimates and updates the system with the time-varying parameters [3]. Some frequently studied parameter estimation techniques include the Yule-Walker (Y-W) estimation method and the least-squares method. The (Y-W) estimator is based on the assumption that, by adjusting an asymptotic bias on the least-squares estimator, a continuous estimator can be obtained. However, the least-squares method is considered to be the most common and most efficient of these parameter estimation techniques. It sets up the system by starting with

the reference model output and following it with the output of the plant to be controlled. The objective is to minimize the least squares criterion, shown in equation (2.10). This criteria is described to be the sum of the squares of the differences between the two outputs, within a specified time interval. This error, between the reference model and plant outputs, is minimized by continuously updating the adaptation mechanism with the controller parameters [3, 15, 31].

$$\min L(t) = \sum_{i=1}^{t} [r(i) - y(i)]^2 \tag{2.10}$$

CHAPTER 3

MODELING

3.1 AMD-1 Schematic and Design Specifications

The Active Mass Damper - One Floor (AMD-1) model, used throughout this thesis work, is composed of four major components. These components include a Quanser VoltPAQ-X1 power amplifier module, a Quanser Q2-USB data acquisition board, a Quanser Active Mass Damper (AMD) plant, and a QUARC real-time control software [29]. An illustration of this experimental setup is shown in Figure 3.1.
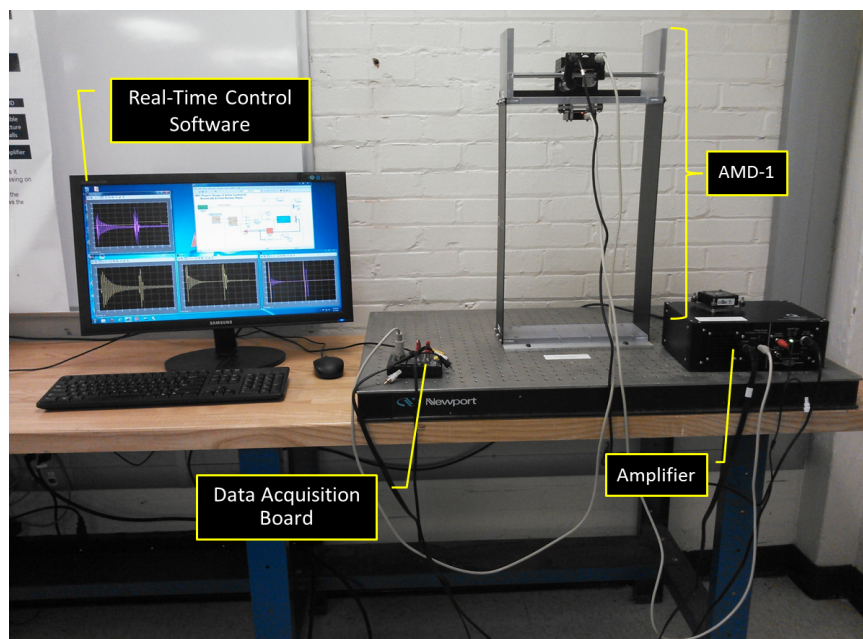
FIGURE 3.1: Experimental setup.

Since it is important for the power amplifier to not go into saturation and for the control effort to stay within the system's physical limitations, the control strategy used the Proportional-Velocity (PV) control scheme. In the AMD mode of the control scheme, the design specifications required the settling time, t_s, to be less than 1 s: $t_s < 1$ s. Also, the flexible structure that the linear cart was mounted on was neglected for all modeling computations [29].

3.2   Equation of Motion

The equations of motion (EOM) for the (AMD-1) system are obtained from the free body diagram. These EOM are validated by comparing them to Quanser's EOM, which was obtained through the Lagrange's method. For both methods, in order to linearly model the system, the Coulomb friction of the cart system is neglected.

When deriving the AMD-1's dynamic model from the free body diagram method, there were two sets of cases considered. The first set of cases considered the cart's driving force, F_c, produced by the motor, to be the system input. It included two cases; one ignored the structure's viscous damping coefficient and the other considered it as an important parameter of the system. Since, Quanser's derivation of the EOM also considered the system input to be F_c and neglected the structure's damping coefficient, the EOM obtained from this set were used for the validating comparison.

The second set included the same cases, but the system input was considered to be the cart motor voltage, V_m. Since all the experimental AMD-1 tests will be using the cart motor voltage as the system input, the EOM obtained from this set were used for all the AMD-1 simulations and experimetnal tests in this thesis work.

3.2.1   Free Body Diagram

Consider the case where the structure's viscous damping coefficient is ignored and F_c is the system input, the corresponding AMD-1 free body diagram is illustrated in Figure 3.2. With the application of Hooke's law and Newton's law of motion, the EOM in equation (3.1a) & (3.1b) was obtained. For simplification, equation (3.1a) was substituted into equation (3.1b) to obtain the EOM in (3.1c).
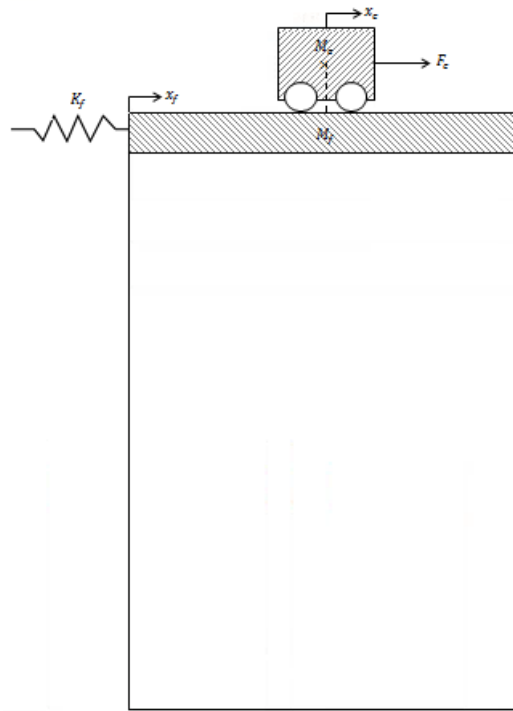
FIGURE 3.2: AMD-1 free body diagram without structure viscous damping.

$$M_f \ddot{x}_f(t) = -K_f x_f(t) - F_c \quad \Longrightarrow \quad \mathbf{\ddot{x}_f(t)} = -\frac{\mathbf{K_f}}{\mathbf{M_f}}\mathbf{x_f(t)} - \frac{\mathbf{F_c}}{\mathbf{M_f}} \tag{3.1a}$$

$$M_c[\ddot{x}_f(t) + \ddot{x}_c(t)] = F_c \quad \Longrightarrow \quad \ddot{x}_c(t) = -\ddot{x}_f(t) + \frac{F_c}{M_c} \tag{3.1b}$$

$$\Longrightarrow \quad \mathbf{\ddot{x}_c(t)} = \frac{\mathbf{K_f}}{\mathbf{M_f}}\mathbf{x_f(t)} + \frac{\mathbf{M_c + M_f}}{\mathbf{M_c M_f}}\mathbf{F_c} \tag{3.1c}$$

Now, consider adding the structure's viscous damping coefficient to the model. The corresponding free body diagram is illustrated in Figure 3.3. The same laws were applied to obtain the dynamic model, but they produced the EOM expressed by equations (3.2a) & (3.2c).
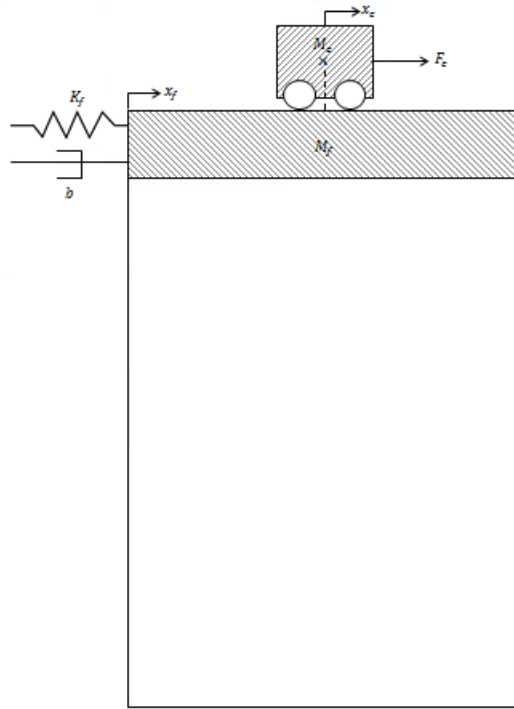
FIGURE 3.3: AMD-1 free body diagram with structure viscous damping.

$$M_f \ddot{x}_f(t) = -K_f x_f(t) - B_f \dot{x}_f - F_c \implies \mathbf{\ddot{x}_f(t)} = -\frac{\mathbf{K_f}}{\mathbf{M_f}}\mathbf{x_f(t)} - \frac{\mathbf{B_f}}{\mathbf{M_f}}\mathbf{\dot{x}_f(t)} - \frac{\mathbf{F_c}}{\mathbf{M_f}} \quad \text{(3.2a)}$$

$$M_c[\ddot{x}_f(t) + \ddot{x}_c(t)] = F_c \implies \ddot{x}_c(t) = -\ddot{x}_f(t) + \frac{F_c}{M_c} \quad \text{(3.2b)}$$

$$\implies \mathbf{\ddot{x}_c(t)} = \frac{\mathbf{K_f}}{\mathbf{M_f}}\mathbf{x_f(t)} + \frac{\mathbf{B_f}}{\mathbf{M_f}}\mathbf{\dot{x}_f(t)} + \frac{\mathbf{M_c + M_f}}{\mathbf{M_c M_f}}\mathbf{F_c} \quad \text{(3.2c)}$$

Next, since the actual input for the experimental testing was the cart motor voltage, V_m, the above "F_c-input" EOM need to be converted into "V_m-input" EOM. According to Quanser, the cart driving force can be expressed by the following "F_c-V_m" relation [29]:

$$F_c = -\frac{\eta_g K_g^2 \eta_m K_m K_t}{R_m r_{mp}^2}\dot{x}_c(t) + \frac{\eta_g K_g \eta_m K_t}{R_m r_{mp}}V_m \quad \text{(3.3)}$$

After substitution and simplification, the "V_m-input" EOM for both cases were obtained. Equations (3.4a) & (3.4b) represent the EOM that ignored the structure viscous damping, and equations (3.5a) & (3.5b) represent the EOM that considered the structure viscous damping coefficient.

$$\ddot{x}_f(t) = -\frac{K_f}{M_f}x_f(t) + \frac{\eta_g K_g^2 \eta_m K_m K_t}{R_m r_{mp}^2 M_f}\dot{x}_c(t) - \frac{\eta_g K_g \eta_m K_t}{R_m r_{mp} M_f}V_m \tag{3.4a}$$

$$\ddot{x}_c(t) = \frac{K_f}{M_f}x_f(t) - \frac{\eta_g K_g^2 \eta_m K_m K_t \left(M_c + M_f\right)}{R_m r_{mp}^2 M_c M_f}\dot{x}_c(t) + \frac{\eta_g K_g \eta_m K_t \left(M_c + M_f\right)}{R_m r_{mp} M_c M_f}V_m \tag{3.4b}$$

$$\ddot{x}_f(t) = -\frac{K_f}{M_f}x_f(t) - \frac{B_f}{M_f}\dot{x}_f(t) + \frac{\eta_g K_g^2 \eta_m K_m K_t}{R_m r_{mp}^2 M_f}\dot{x}_c(t) - \frac{\eta_g K_g \eta_m K_t}{R_m r_{mp} M_f}V_m \tag{3.5a}$$

$$\ddot{x}_c(t) = \frac{K_f}{M_f}x_f(t) + \frac{B_f}{M_f}\dot{x}_f(t) - \frac{\eta_g K_g^2 \eta_m K_m K_t \left(M_c + M_f\right)}{R_m r_{mp}^2 M_c M_f}\dot{x}_c(t) + \frac{\eta_g K_g \eta_m K_t \left(M_c + M_f\right)}{R_m r_{mp} M_c M_f}V_m$$

$$\tag{3.5b}$$

3.2.2 Lagrange's Method

Quanser's Lagrangian approach was used to validate the EOM obtained from the free body diagram. In this approach, the AMD-1 structure was modeled as a linear spring-mass system with F_c as the single input to the system [29].

The Lagrangian, expressed as the difference between the system's total kinetic and potential energies, is expressed by equation (3.6).

$$L = T_T - V_T. \tag{3.6}$$

Since the motorized linear cart's translational direction is orthogonal to the rotor's rotation, the system's total kinetic energy, T_T, is expressed as the sum of the cart's translational kinetic

energy, Tt_c, the rotational kinetic energy of the cart motor, Tr_c, and the translational kinetic energy of the flexible structure's floor, Tt_f. This summation is shown below:

$$T_T = Tt_c + Tr_c + Tt_f \tag{3.7a}$$

$$T_T = \left[\frac{1}{2}M_c\left(\dot{x}_c(t) + \dot{x}_f(t)\right)^2\right] + \left[\frac{1}{2}\frac{J_m K_g^2}{r_{mp}^2}\ddot{x}_c(t)\right] + \left[\frac{1}{2}M_f\ddot{x}_f(t)\right] \tag{3.7b}$$

By combining like terms, equation (3.7b) can be simplified to the folowing expression:

$$T_T = \left(\frac{r_{mp}^2 M_c + J_m K_g^2}{2r_{mp}^2}\right)\ddot{x}_c(t) + M_c\dot{x}_f(t)\dot{x}_c(t) + \left(\frac{M_c + M_f}{2}\right)\ddot{x}_f(t) \tag{3.8}$$

The AMD-1's total potential energy, V_T, is only expressed by the elastic potential energy, because the gravitational potential energy is assumed to be negligible. That being said, the system's total potential energy is expressed as:

$$V_T = \frac{1}{2}K_f x_f(t)^2 \tag{3.9}$$

Recalling the system's schematic, represented by the free body diagrams, it is determined that the system has two Degrees-of-Freedom (DOF). It was for this reason that the system should have two Lagrangian (generalized) coordinates, which were chosen to be: x_c and x_f. Furthermore, the system's Lagrange equations are expressed as:

$$\left(\frac{\partial}{\partial t \partial \dot{x}_c(t)}L\right) - \left(\frac{\partial}{\partial x_c(t)}L\right) = Q_{x_c} \tag{3.10a}$$

$$\left(\frac{\partial}{\partial t \partial \dot{x}_f(t)}L\right) - \left(\frac{\partial}{\partial x_f(t)}L\right) = Q_{x_f} \tag{3.10b}$$

With the Lagrangian known, the only remaining unknown variables in the Lagrange's equations are the system's generalized forces. The nonlinear Coulomb friction, applied to the linear cart, and the viscous damping force, applied to the structure floor, are neglected, which resulsts in the generalized forces expressed below:

$$Q_{x_c}(t) = F_c - B_{eq}\dot{x}_c(t) \tag{3.11a}$$

$$Q_{x_f}(t) = 0 \tag{3.11b}$$

The Lagrangian equation (3.6) and the generalized forces (3.11) are substituted into the Lagrange's equations, (3.10), to produce a more explicit expression of the first and second Lagrange's equations. The EOM was obtained when the Lagrange's equations were solved for the second-order time derivative of the two Lagrangian coordinates. This result is represented below.

$$\ddot{x}_c(t) = \frac{K_f M_c r_{mp}^2 x_f(t) + r_{mp}^2(-M_c B_{eq} - M_f B_{eq})\dot{x}_c(t) + r_{mp}^2(M_c + M_f)F_c}{M_c r_{mp}^2 M_f + J_m K_g^2 M_c + J_m K_g^2 M_f} \tag{3.12a}$$

$$\ddot{x}_f(t) = \frac{K_f(M_c r_{mp}^2 + J_m K_g^2)x_f(t) + M_c B_{eq} r_{mp}^2 \dot{x}_c(t) - M_c r_{mp}^2 F_c}{M_c r_{mp}^2 M_f + J_m K_g^2 M_c + J_m K_g^2 M_f} \tag{3.12b}$$

As a remark, when the equivalent viscous damping coefficient, B_{eq}, as seen at the motor pinion, and the cart rotor's moment of inertia, J_m, are neglected, the EOM becomes:

$$\ddot{x}_c(t) = \frac{K_f}{M_f}x_f(t) + \frac{M_c + M_f}{M_c M_f}F_c \tag{3.13a}$$

$$\ddot{x}_f(t) = -\frac{K_f}{M_f}x_f(t) - \frac{1}{M_f}F_c \tag{3.13b}$$

Notice, when the above EOM, (3.13), is compared to the EOM in (3.1), obtained from the first case of the free body diagram method, they are found to be identical! That being said, validation is achieved for all EOM obtained from the free body diagram.

CHAPTER 4

SIMULATION

MATLAB and Simulink were used to simulate the response of the AMD-1 system and measure its response throughout the experimental testing. In order for these programs to interpret the mathematically derived model of the system, it must be converted into its state-space representation. That is to say, the state-space matrices $\mathbf{A}$, $\mathbf{B}$, $\mathbf{C}$, and $\mathbf{D}$ must be determined in a way that satisfies the expression in (4.1).

$$\dot{\mathbf{x}}(t) = \mathbf{A}\mathbf{x}(t) + \mathbf{B}u \tag{4.1a}$$

$$\mathbf{y}(t) = \mathbf{C}\mathbf{x}(t) + \mathbf{D}u \tag{4.1b}$$

The state variables, $\mathbf{x}$, were chosen to be the generalized coordinates (x_c and x_f) and their first-order time derivatives. The desired outputs, $\mathbf{y}$, were chosen to be the cart position, x_c and the floor acceleration, x_f. These states were chosen to be the outputs, because they can be more easily measured in a real-life situation than any of the others. Now, recall the "V_m"-EOM, obtained in the previous section, by rearranging and organizing the variables appropriately, the state space matrices can be determined. The corresponding state-space representation of the

"V_m-input" EOM is shown in equation (4.2).

$$
\begin{bmatrix} \dot{x}_c(t) \\ \dot{x}_f(t) \\ \ddot{x}_c(t) \\ \ddot{x}_f(t) \end{bmatrix} = \begin{bmatrix} 0 & 0 & 1 & 0 \\ 0 & 0 & 0 & 1 \\ 0 & \frac{K_f}{M_f} & -\frac{(M_c+M_f)K_g^2 K_t K_m}{M_c M_f R_m r_{mp}^2} & 0 \\ 0 & -\frac{K_f}{M_f} & \frac{K_g^2 K_t K_m}{M_f R_m r_{mp}^2} & -\frac{B_f}{M_f} \end{bmatrix} \begin{bmatrix} x_c(t) \\ x_f(t) \\ \dot{x}_c(t) \\ \dot{x}_f(t) \end{bmatrix} + \begin{bmatrix} 0 \\ 0 \\ \frac{(M_c+M_f)K_g K_t}{M_c M_f R_m r_{mp}} \\ -\frac{K_g K_t}{M_f R_m r_{mp}} \end{bmatrix} V_m \qquad (4.2a)
$$

$$
\begin{bmatrix} x_c(t) \\ \ddot{x}_f(t) \end{bmatrix} = \begin{bmatrix} 1 & 0 & 0 & 0 \\ 0 & -\frac{K_f}{M_f} & \frac{K_g^2 K_t K_m}{M_f R_m r_{mp}^2} & -\frac{B_f}{M_f} \end{bmatrix} \begin{bmatrix} x_c(t) \\ x_f(t) \\ \dot{x}_c(t) \\ \dot{x}_f(t) \end{bmatrix} + \begin{bmatrix} 0 \\ -\frac{K_g K_t}{M_f R_m r_{mp}} \end{bmatrix} V_m \qquad (4.2b)
$$

4.1 MATLAB Simulations

The obtained state-space matrices and the system's physical constants, which are documented in the front matter under **Physical Constants**, are defined in MATLAB with the script 'Vm_SYSTEM.m,' found in Appendix A. Figure (1) and (2) of this code produce the steady state response of the system obtained from a step input and an impulse input, respectively. The step input represents a constant application of the input voltage, while the impulse input represents a quick jolt. The simulated responses obtained from each input are illustrated in Figure 4.1, with the step response on the top and the impulse response on the bottom.

These plots provide a visual explanation of how the raw system should react to a given input. With a step input, the cart position response was found to be unstable, as it linearly increased to infinity. This was expected because the constantly applied voltage is directly related to the cart position, as seen in the state-space representation. The step input's floor acceleration response, on the other hand, was stable. This is because the floor acceleration is represented
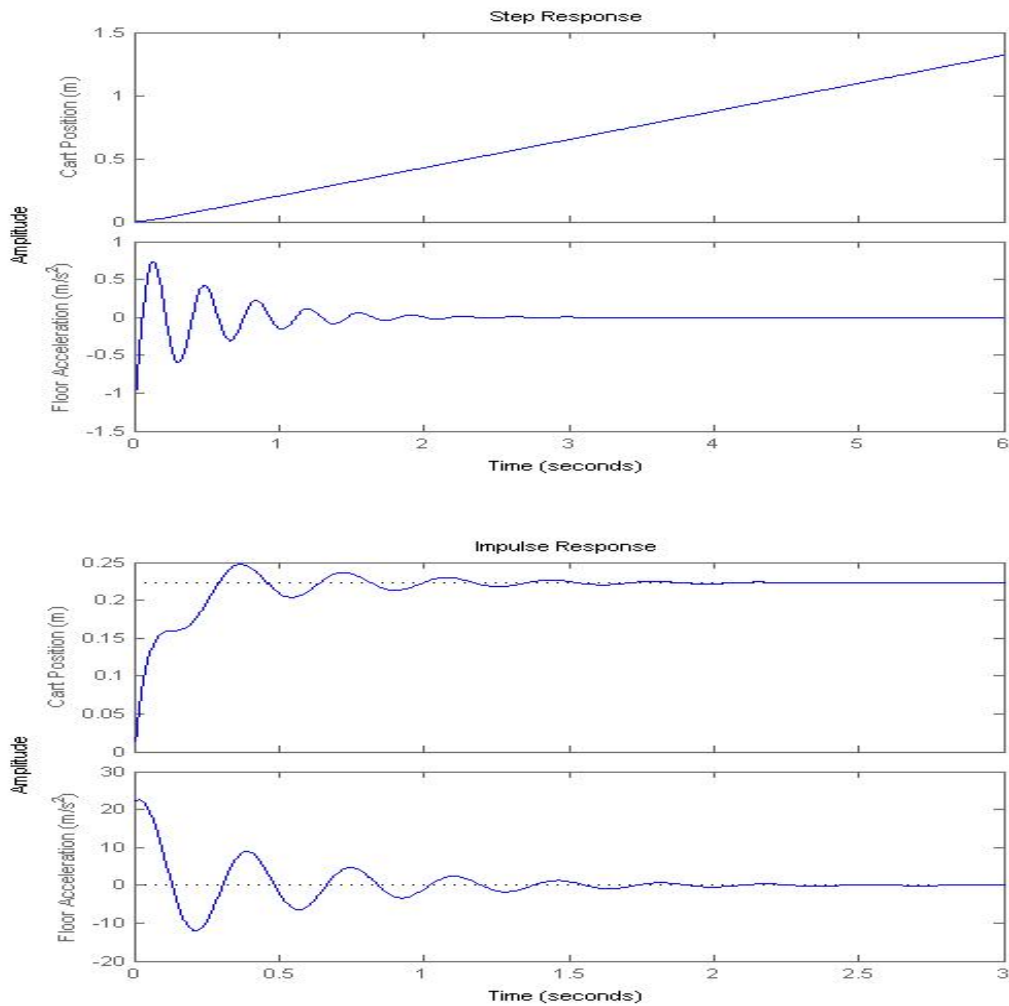
FIGURE 4.1: The system's natural step response (top) and impulse response (bottom).

by variables that take into account the damping effect of cart on the system. With an impulse input, the cart position and floor acceleration response were both found to be stable, which is simply an effect of the temporarily applied voltage.

4.1.1 Controllability and Observability

A control system was designed and implemented to improve the system's output response based on its input and its ability to estimate the state variables from the outputs. In

order for this control system to be viable, it must be confirmed that the system is both control-lable and observable.

A system is controllable if and only if, in a definite time interval, its states can be modified by varying the input. This is confirmed when, the controllability matrix, **CO**, has full rank. In other words, its rank must be equal to the number of system states [7, 21].

$$\mathbf{CO} = \begin{bmatrix} \mathbf{B} & \mathbf{AB} & \mathbf{A}^2\mathbf{B} & \mathbf{A}^3\mathbf{B} \end{bmatrix} \tag{4.3}$$

A system is observable if and only if its states can be interpreted from its outputs. The observability matrix, **W**, is used to verify this ability. Again, confirmation is achieved only when the observability matrix has full rank [7, 21].

$$\mathbf{W} = \begin{bmatrix} \mathbf{C} & \mathbf{CA} & \mathbf{CA}^2 & \mathbf{CA}^3 \end{bmatrix}^T \tag{4.4}$$

Both the controllability and observability matrices were computed for the AMD-1 sys-tem, and were confirmed to have full rank, verifying that the system can be both controlled and observed. Control was achieved through the state-feedback design and observability was achieved through the full-order state observer design.

4.1.2   State-Feedback Design

The state-feedback design uses a full-state feedback gain vector, **K**, to control a system by placing the system's closed-loop poles at the desired pole locations. Vector **K** is designed to satisfy equation (4.5), which controls the system input. After implementation of this gain into the system, the new and improved system takes the form of equation (4.6), where the eigenvalues of $(\mathbf{A} - \mathbf{BK})$ represent the system's closed-loop poles.

$$u = \mathbf{Kx} \tag{4.5}$$

$$\dot{\mathbf{x}} = (\mathbf{A} - \mathbf{BK})\mathbf{x} \tag{4.6}$$

The desired locations for these closed-loop pole are determined by the system's desired time-domain specifications. Due to the state-feedback law, these poles were placed at the following locations:

$$\mathbf{P} = \begin{bmatrix} -6+15j & -6-15j & -8 & -16 \end{bmatrix}$$

To show why these poles were chose, recal the characteristic equation of a standard second-order system and its characteristic roots:

$$s^2 + 2\zeta \omega_n s + \omega_n^2 = 0 \tag{4.7a}$$

$$s = -\zeta \omega_n \pm j\omega_n \sqrt{1-\zeta^2} \tag{4.7b}$$

The system's damping ratio, ζ, and natural frequency, ω_n, are used to determine whether or not the system response is satisfactory, with respect to the desired time-domain specifications. With a plot of the system's dominant pole, in the complex plane, these parameters can be calculated. From vector $\mathbf{P}$, it is established that "$-6 \pm 15j$" is the dominant pole because e^{-6} has a slower decay rate than e^{-8} and e^{-16}, thus having a greater influence on the system response. The corresponding plot of this pole's location is illustrated in Figure 4.2.

From this plot and With the use of trigonometry, the system's parameters (ζ and ω_n) are determined from the pole's location. Table 4.2 contains the calculated values of ζ and ω_n, along with the equations used to obtain those values.

Finally, the current system's AMD-mode time-domain specifications can be determined from these known parameters. Table 4.2 contains the calculated values for each specification
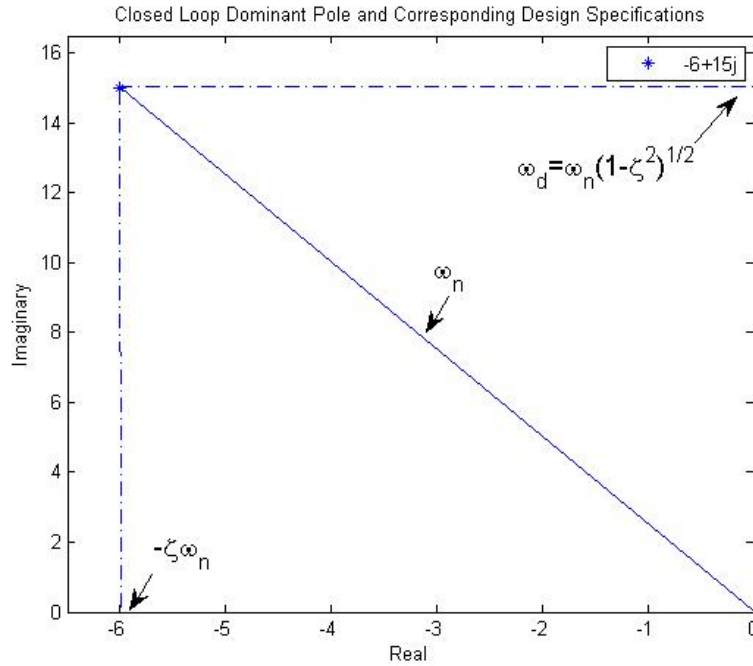
FIGURE 4.2: A plot of the system's dominant pole and the corresponding system parameters.

TABLE 4.1: System Parameters Obtained from the Pole Plot

Specification	Equation	Value
Natural Frequency	$\text{Re}^2 + \text{Im}^2 = \omega_n^2$	$\omega_n = 16.1555$ Hz
Damping Ratio	$\text{Re} = \omega_n \zeta$	$\zeta = .37139$

along with the formulas used to obtain them. Recall the AMD-mode settling time design specification: $t_s \leq 1s$, stated in the previous section titled *Experimental Setup and Specifications*. From the table's settling time value, it is concluded that the system's peak time performance was satisfactory because it settled in about .6667 s, which is faster than specified.

TABLE 4.2: Time-Domain Specifications Obtained from the System Parameters

Specification	Equation	Value
Settling Time	$t_s = \frac{4}{\zeta \omega_n}$	$t_s = .667$ s
Peak Time	$t_p = \frac{\pi}{\omega_n \sqrt{1-\zeta^2}}$	$t_p = .209$ s
Percent Overshoot	$M_p = e^{\left(\frac{-\pi\zeta}{\sqrt{1-\zeta^2}}\right)}$	$M_p = 28.461$ %

The full-state feedback gain vector, **K**, shown below, was determined by the use of the MATLAB 'place' command. This is also shown in the MATLAB script 'Vm_SYSTEM.m', found in Appendix A, where the system was updated with the feedback gain vector and its figure (3) and (4) are used to simulated the controlled response. These new controlled step (top) and impulse (bottom) responses are shown in Figure 4.3.

$$\mathbf{K} = \begin{bmatrix} 45.0945 & -213.8050 & 4.3052 & -4.5640 \end{bmatrix} \tag{4.8}$$
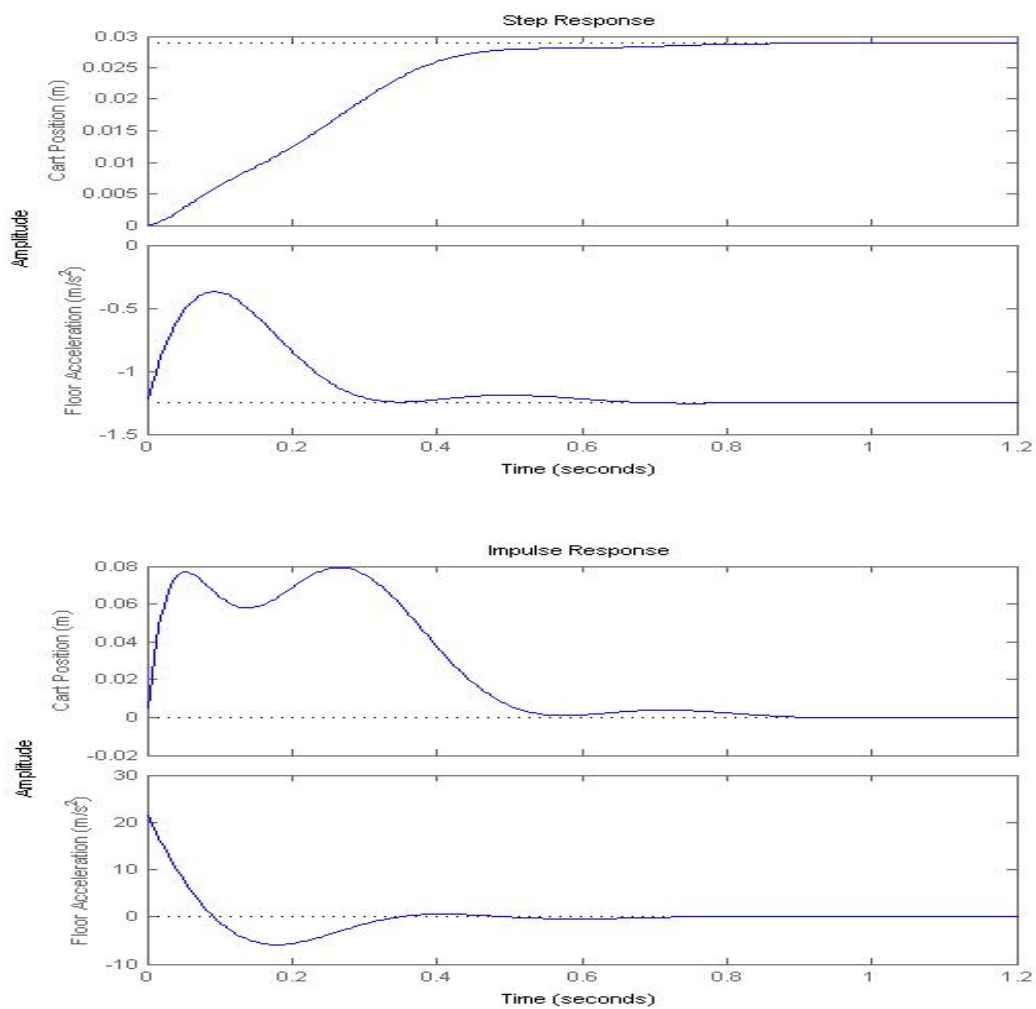
FIGURE 4.3: The system's controlled step response (top) and impulse response (bottom).

A comparison of these controlled responses with the natural responses, of Figure 4.1, indicates that the use of vector **K** was successful. First consider the responses obtained from the step input (a constant voltage). The natural cart position response was unstable, but when the feedback gain is applied to the system, its response is stabilized, leveling off at about .o3 m. The floor acceleration response, although already stable in its natural state, showed an improved decay rate with the application of the feedback gain. The natural floor acceleration response took about 3 s to decay, but after the feedback gain was added, it decayed in less than 1 s.

Now consider the responses obtained from the impulse input (a voltage jolt). The natural response of the cart position peaked at .25 m and only decayed to about .225 m. With the feedback gain, the peak only reached .08 m and it decayed all the way to 0 m. Just as in the step responses, the effect of the feedback gain, on the floor acceleration was an improved decay rate. It decreased its decay time from 3 s to about .8 s.

4.1.3   Full-Order State Observer Design

According to the full-state feedback law, since only the floor acceleration is directly measured, the AMD-1's active control strategy should also incorporate a state observer. This design specification was chosen to more accurately represent a full-scale application, where the floor deflection or velocity are very difficult to measure. Accelerometers, provide affordable and reliable means of sensing a structure's dynamic behavior, and they produce measurements that can be used to estimate the floor deflection and velocity.

The observer is designed to satisfy equation (4.9), and is essentially a replica of the actual plant, but with a corrective term that gets multiplied by the full-order observer gain

matrix, $\mathbf{G}$.

$$\dot{\mathbf{X}}_0 = \mathbf{A}\mathbf{X}_0 + \mathbf{B}\mathbf{U} + \mathbf{G}(\mathbf{Y} - \mathbf{Y}_0) \tag{4.9a}$$

$$\mathbf{Y}_0 = \mathbf{C}\mathbf{X}_0 + \mathbf{D}\mathbf{U} \tag{4.9b}$$

Vector $\mathbf{G}$ was determined by placing the closed-loop poles at the locations specified by vector $\mathbf{OP}$. These locations were chosen based on the observer error dynamics. It ensures that there will be no interference from the observer on the plant's dynamics, and was chosen to make the observer error dynamics over three times faster than the plant's error dynamics.

$$\mathbf{OP} = \begin{bmatrix} -20 & -25 & -30 & -35 \end{bmatrix}$$

The MATLAB script 'Vm_SYSTEM.m', found in Appendix A, was also used to determine the value of the full-order observer gain matrix, $\mathbf{G}$, and to update the system with the observer gain. Visual plots illustrating the actual and estimated states will be provided in the Simulink section.

$$\mathbf{G} = \begin{bmatrix} 36.6829 & 0.0036 \\ -4.7604 & -0.1765 \\ 107.6736 & -0.7844 \\ -243.1164 & -1.5950 \end{bmatrix} \tag{4.10}$$

4.2 Simulink Simulations

To accompany and support the above MATLAB responses, corresponding Simulink diagrams were constructed for the system's response to a step-input. The open-loop, closed-loop, and state observer diagrams are presented and used to simulate and analyze the system's output responses.

4.2.1 Open-Loop

Figure 4.4 represents the open-loop model of the AMD-1 system. The state-space matrices ($\mathbf{A}$, $\mathbf{B}$, $\mathbf{C}$, and $\mathbf{D}$) were uploaded, with the previously mentioned MATLAB scripts, and the scope was used to plot its response.
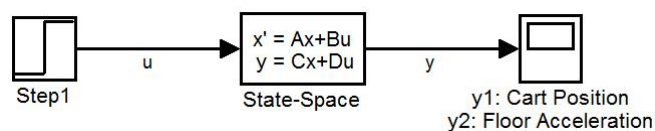
FIGURE 4.4: Open-loop Simulink diagram.

Figure 4.5 illustrates the response of the open-loop system. Notice, both the cart position and floor acceleration responses perfectly match those obtained from the MATLAB code, but they are plotted on the same graph. Just the same, the cart's position response is unstable, increasing toward infinity, and the floor acceleration response is stable, decaying over time.

4.2.2 Closed-Loop - Feedback Controller

Just as before, the system needs to be controlled. Control is achieved by adding the feedback gain, $\mathbf{K}$, to the system. Doing so, resulted in the closed-loop Simulink diagram, illustrated in Figure 4.6. Again, the corresponding state space matrices and feedback gain vector were uploaded, and the scope was used to plot the system's response.

Figure 4.7 illustrates the controlled response obtained from the closed-loop system. Again, both output responses were proved to be identical to those obtained from the MATLAB
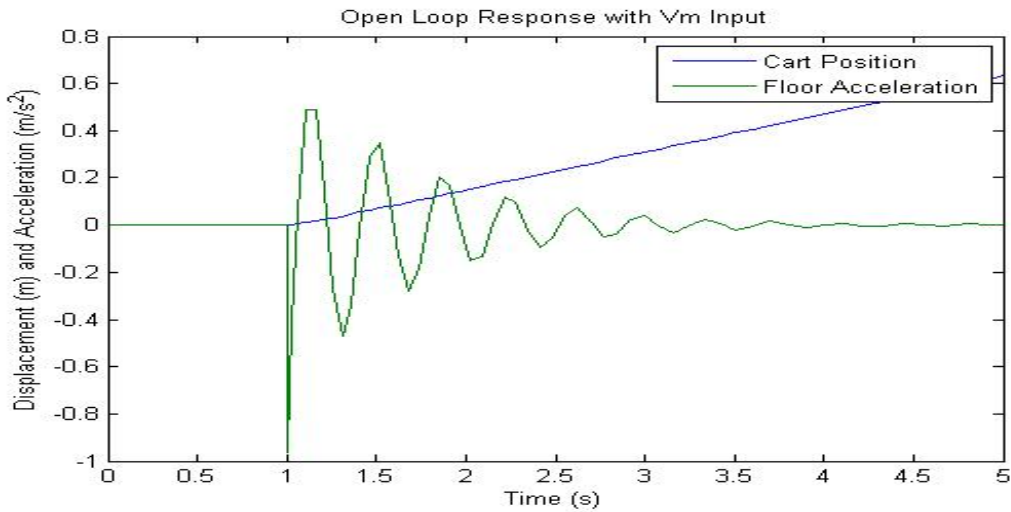
FIGURE 4.5: Open-loop scope of the system's response.
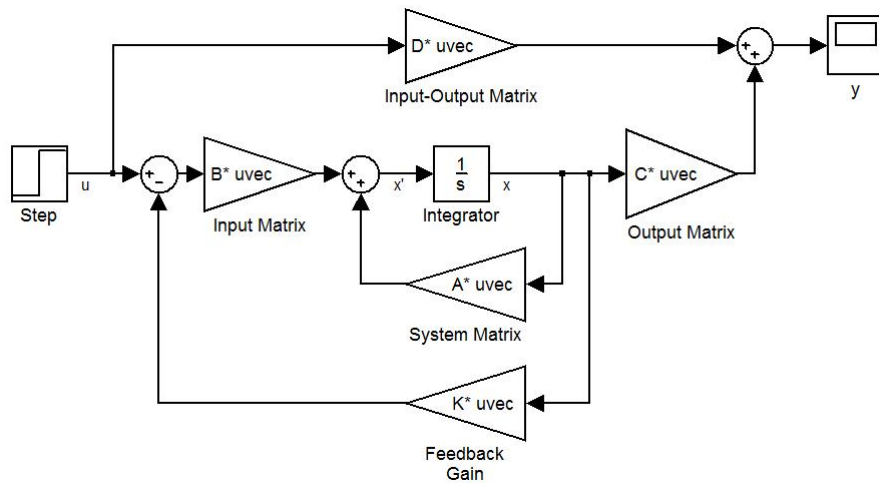
FIGURE 4.6: Closed-loop Simulink diagram.

code. Just the same, the cart's position response was stabilized and the floor acceleration response's decay rate was increased. These similarities confirm the consistency of the derived mathematical model.

4.2.3   Closed-Loop - Feedback Controller with an Observer

Lastly, the system with the state observer was modeled. The corresponding state observer Simulink Diagram is shown in Figure D.1 of Appendix D, where the plant, observer plant, controller feedback, and observer feedback are all present. To obtain a smoother, more
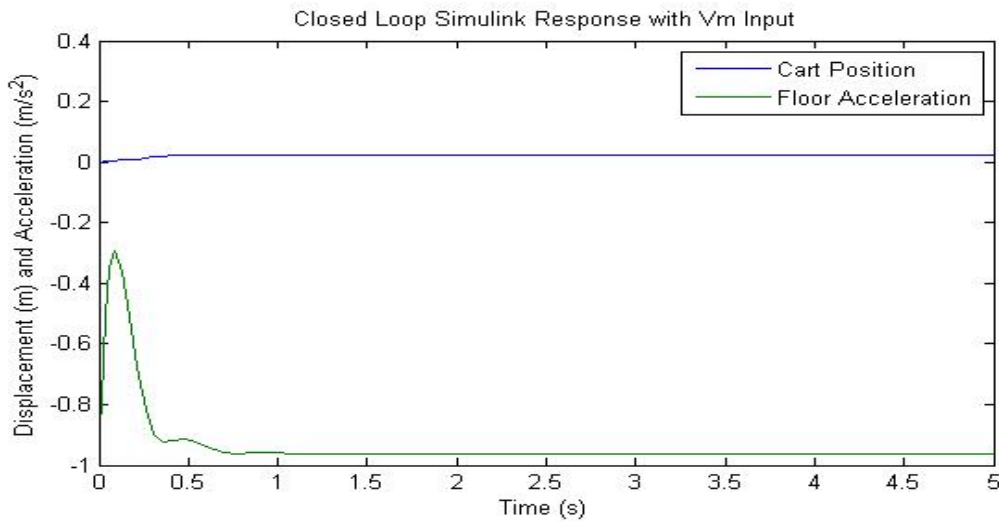
FIGURE 4.7: Closed-loop scope of the system's response.

distinguished response, the step input was replaced with a 2.5 Hz frequency sine wave of amplitude .02. Also, for better visualization and understanding of the benefits gained from utilizing a state observer, an initial condition was placed on the main plant. This condition consisted of an initial floor position of 3 mm. On the contrary, the observer plant's initial conditions were all kept at zero . Also, present in this diagram are multiple scopes that were used to plot the following responses: the plant's output, 'y', the observer plant's output, '$\bar{y}$', plant's states, 'x', the estimated observer plant's states, '$\bar{x}$', and the system error, '$y - \bar{y}$'.

Figure 4.8 illustrates the comparison of the plant's states, x, and the estimated observer plant's states, $\bar{x}$. Notice that both plants produce identical responses for both the cart's position and velocity. The floor's position and velocity, on the other hand, are similar, yet not identical. The plant's initial floor position of 3 mm, explains why the floor position responses had different initial values; however, its observed that it only took about .05 s for the two responses to converge. A similar effect from the initial condition was seen in the floor velocity response, but it took about .3s to converge. This suggests that the higher derivative of the velocity intensified the discrepancy by about 6 times that of the floor position.

Figure 4.9 illustrates the comparison of the plant's output, y, and the observer plant's output, $\bar{y}$, response. It is observed that the both plants produced identical cart position output
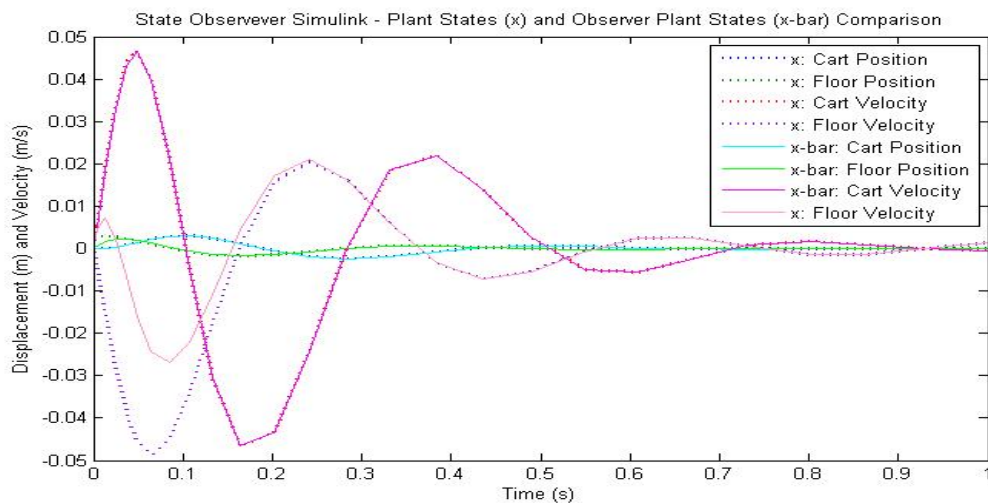
FIGURE 4.8: State observer Simulink - a comparison of the plant's and observer plant's state responses.

responses, but different, yet similar, floor acceleration output responses. Likewise, this small deviation, in the beginning of the floor acceleration responses, is an effect of the different initial conditions. Notice though, even with different initial conditions, these responses still converge to the same trajectory after only 25 s.
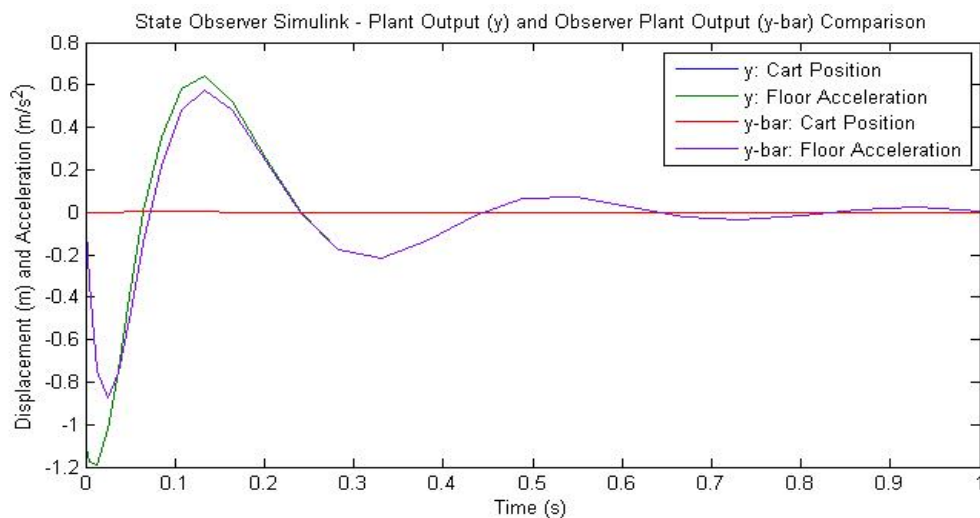
FIGURE 4.9: State observer Simulink - a comparison of the plant's and observer plant's output responses.

Finally, figure 4.10 illustrates the system's error, denoted by $y - \bar{y}$, which represents the difference between the plant's output and the observer plant's output. Notice, the cart's
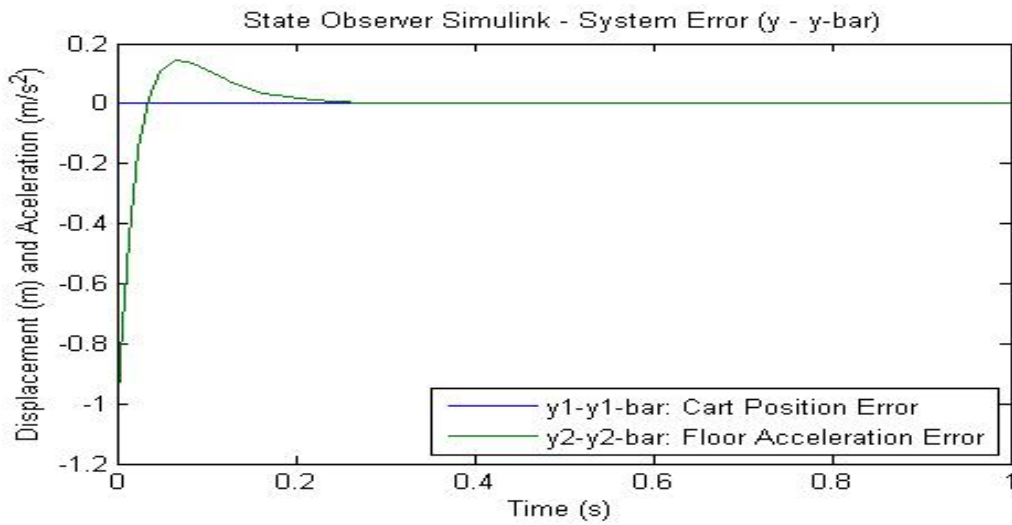
FIGURE 4.10: State observer Simulink - system's error.

position's error is zero, which implies that these response are exactly the same for both plants. On the contrary, the floor acceleration error, showed some discrepancy. However, the main point is, despite having different initial conditions, the error still converges to zero, and does so in just over .3 s. These observations come as no surprise since they are completely supported by the conclusions made from previous output comparison plot.

CHAPTER 5

PARAMETER ESTIMATION

Since the viscous damping coefficient of the structure, B_f, was neglected in all the previous simulations, parameter estimation techniques were used to obtain a more accurate model of the system. The two techniques considered for this estimation included a Simulink Parameter Estimation Toolbox and an external motion and force sensor.

5.1 Simulink Toolbox

Figure 5.1 illustrates the Simulink diagram that incorporated the Simulink Parameter Estimation Toolbox. It included a basic model of the AMD-1's mass-spring-damper system, a 'Parameter Estimation GUI with preloaded data' toolbox, a transient data block, and a system parameter block, which contains their current values. Within the transient data block was preloaded floor position data that was obtained from an experimental test on the AMD-1 structure. The scope, shown in Figure 5.2, illustrates the plots of the unstable simulated floor position response and the preloaded experimental floor position data, both of which had an initial floor position of 12.0126 mm.

The presented GUI toolbox contained a 'Control and Estimation Tools Manager,' which is where the parameter estimation project was created. It performed a number of continuous parameter estimation iterations until the simulated response converged to take a form similar to response produced by the transient data. In this case, the estimation tool performed 100 iterations, where the final values of the estimated parameters were: $M_f = 2.509$ kg, $B_f = 3.283$ Ns/m, and $K_f = 511.9$ N/m. The resultant plot of the estimator is plotted with the transient data in Figure 5.3, where it is observed that the two responses very closely resemble each other.
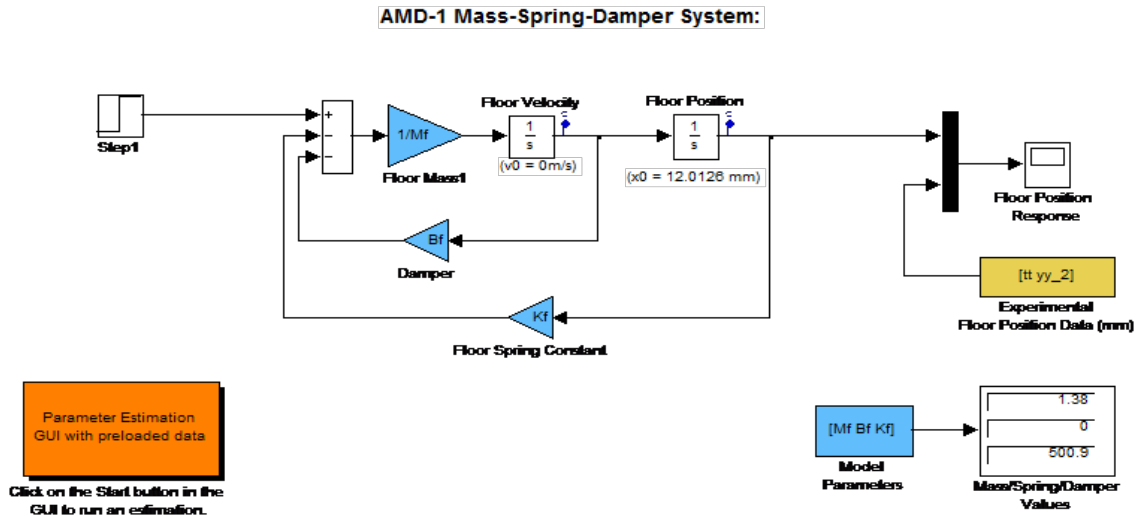
FIGURE 5.1: Simulink model of the AMD-1's mass-spring-damper system with parameter estimation GUI.
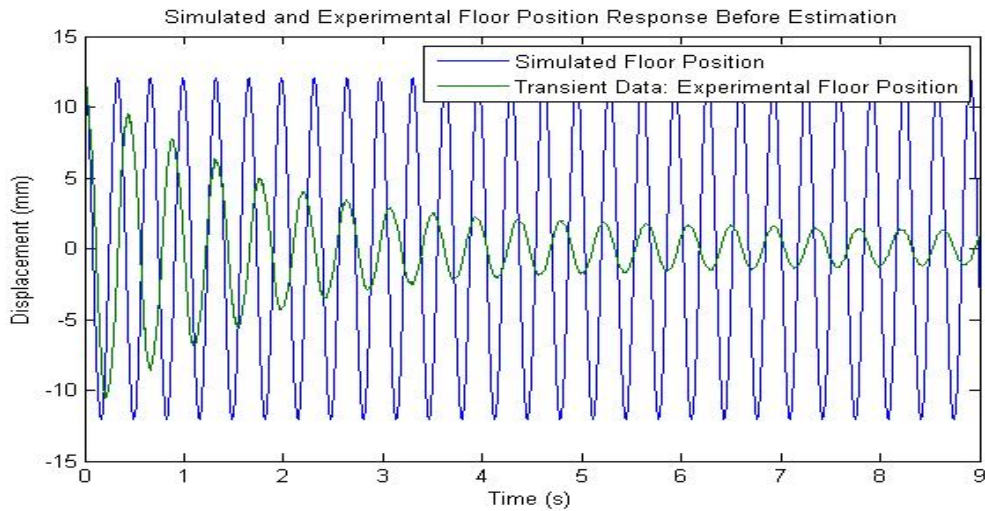
FIGURE 5.2: A comparison of the simulated and experimental floor position data before estimation.

5.1.1 External Sensor Tests

An external motion and force sensor was also used to estimate the system parameters. The setup of these sensors, with respect to the AMD-1 model, is illustrated in Figure 5.4. Here, the motion sensor was supported by a tripod, which was positioned at the height of the AMD-1's top floor, and the force sensor, was tied to the top of the structure's wall with fishing line. In
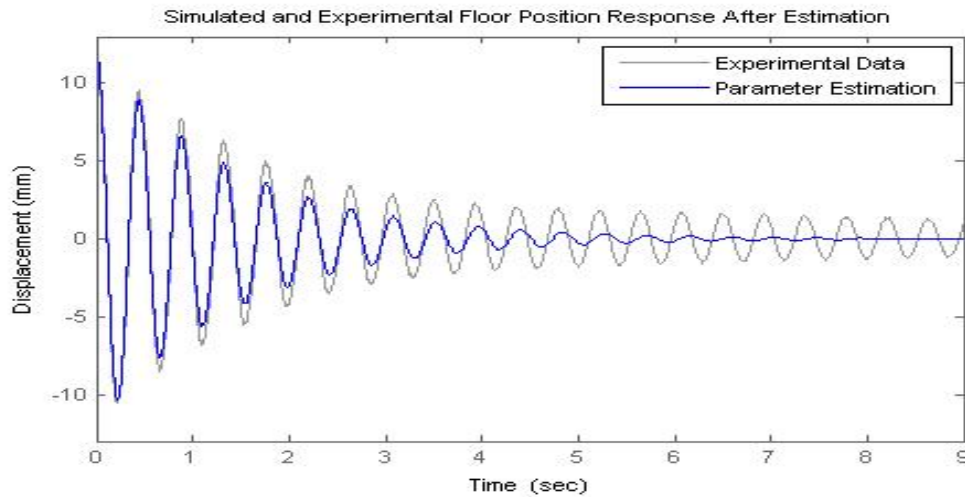
FIGURE 5.3: A comparison of the experimental and estimated floor position response after estimation.

addition, both sensors were connected to the computer, where real-time data was unanimously collected.
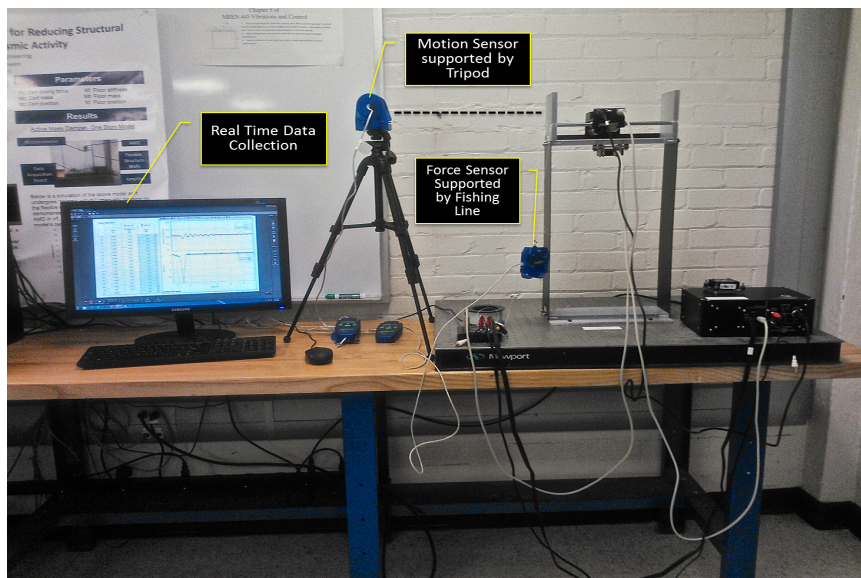
FIGURE 5.4: Force and motion sensor setup.

With both sensors turned on, an impulse excitation was applied to the AMD-1 structure by quickly pulling the force sensor away from the model and immediately letting go. A plot of the collected sensor data is illustrated in Figure 5.5, where the data tips represent the important values that were used to calculate the system parameters. From this data K_f was derived from

Hooke's law, M_f was derived from the natural frequency formula, and B_f was derived from the logarithmic decrement.
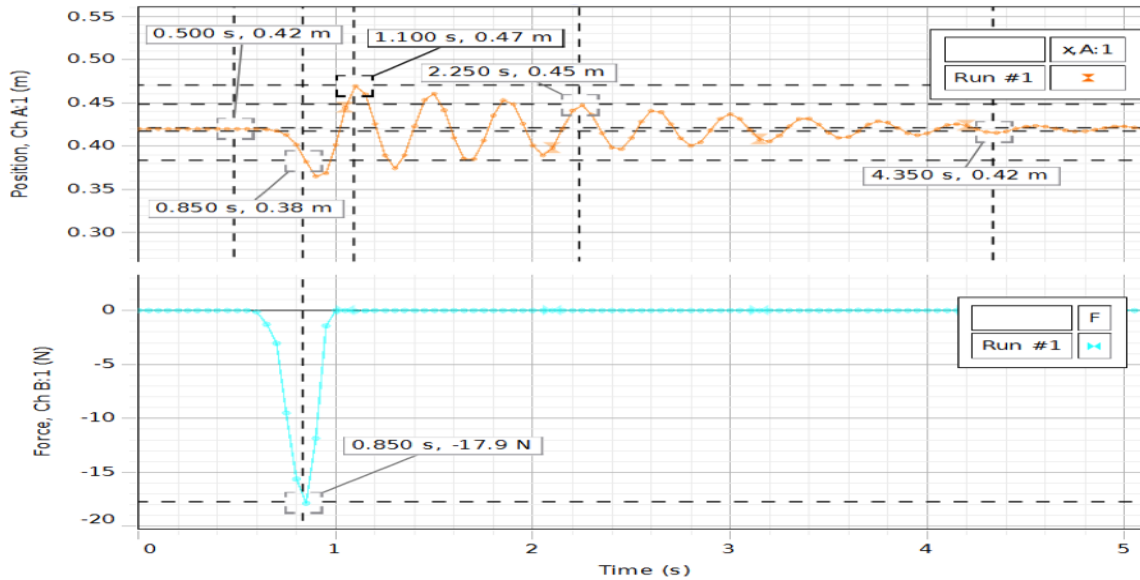
FIGURE 5.5: Force and motion sensor response as an impulse force was applied to the AMD-1 structure.

Table 5.1 organizes and defines the variables obtained from the sensor data and the calculations used to derive K_f and M_f. From the force sensor's plot, the maximum applied force, F_{max}, was easily found by the value at the tip of the single peak. Note, the reason that this peak is negative is simply because the force sensor was pulled to the left. The time at which this maximum force was applied was used to obtain the corresponding floor position, x_{force}. However, this position is not the actual displacement of the floor. Notice, at rest, the sensor data shows that the floor position is at .42 m, which is the distance between the sensor and the floor. Therefore, that distance must be subtracted from x_{force} to get the actual displacement of the floor. This value, along with F_{max} was used in Hook's law to calculate K_f.

Next, the period, T, of the position sensor's response was measured and used to calculate the natural frequency of the system, ω_n. This value, along with the previously calculated stiffness, were used to obtain Mf with the natural frequency formula expressed in Table 5.1.
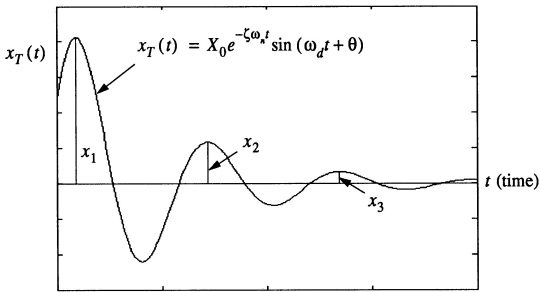
Table 5.2 formulates the derivation of B_f. Presented is the calculation of the system's free response. From this response, the logarithmic decrement, δ, was found, which is defined

TABLE 5.1: Derivation of the Floor's Stiffness and Mass

Variable	Symbol	Value	Calculations
Maximum Force Applied	F_{max}	-17.8629 N	$F = kx$
Distance Between Sensor and AMD-1	x_s	.42 m	$K_f = \frac{F_{max}}{x_{force} - x_s}$
Floor Position at Time of F_{max}	x_{force}	.382 m	$\mathbf{K_f = 470.0763 \ N/m}$
Period	T	.375 s	$\omega_n = \sqrt{\frac{K_f}{M_f}}$
Frequency	$f = 1/T$	8/3 Hz	$M_f^2 = \frac{K_f}{M_f^2}$
Natural Frequency	$\omega_n = 2\pi f$	$\frac{16\pi}{3}$ rad/s	$\mathbf{M_f = 1.6744 \ kg}$

as the natural logarithm of the ratio of two consecutive amplitudes. The value of δ was obtained through the graphical approach, which uses the measurements of peak one and six (shown by the data tips in Figure 5.5). With this value, the damping ratio was calculated through the numerical approach. Then finally, with the damping ration, the floors mass, and the floors stiffness, B_f was determined.

TABLE 5.2: Derivation of the Floor's Damping Coefficient, Graph: [18]

Calculation of the System's Free Response:	$m\ddot{x} + 2\zeta\omega_n\dot{x} + \omega_n^2 x = 0$ $x_T(t) = X_0 e^{-\zeta\omega_n t}\sin(2\pi f t + \phi)$
Logarithmic Decrement: 	$\delta = \ln\frac{x(t)}{x(t+T)}$ Graphical Approach Numerical Approach $\delta = \frac{1}{n}\ln\frac{x_1}{x_{n+1}}$ $\delta = \ln\frac{2\pi\zeta}{\sqrt{1-\zeta^2}}$ $\delta = \frac{1}{5}\ln\frac{.469 - .42}{.437 - .42}$ $\zeta = \frac{\delta}{\sqrt{4\pi^2+\delta^2}}$ $\delta = .2117 \longrightarrow$ $\zeta = \frac{.2117}{\sqrt{4\pi^2 + .2117^2}}$ $\zeta = .03368$ $B_f = 2\zeta\sqrt{M_f K_f}$ $\mathbf{B_f = 1.8898 \ Ns/m}$

In the graph: $x_T(t)$, $x_T(t) = X_0 e^{-\zeta\omega_n t}\sin(\omega_d t + \theta)$, x_1, x_2, x_3, t (time)

CHAPTER 6

RESULTS

6.1 Experimental Testing

All the experimental tests were performed on a single story building model. Recall Figure 3.1, where it shows the AMD-1 model connected to a computer installed with the real-time control software, QUARC. This software was used in the Simulink Model, shown in Figure D.2 of Appendix D, to run the experimental tests and collect the response data, which included the floor's position and acceleration, the cart motor voltage, and the cart position.

To obtain these responses, the necessary system parameter and state-space matrix values were defined within the Simulink model with a provided set of MATLAB scripts [29]. As improvements were made to the system, these scripts were updated and modified with the MATLAB scripts documented in the Appendix.

Notice, the mode switching sequence incorporated in this model. It is used to alternate between the structure excitation mode and the active mass damping mode. Initially, this sequence was programmed to excite the AMD-1 structure at 0 s, and again at 11.5 s, and then also dampen it at 11.5 s. In other words, the controller was off during the first excitation, and then turned on, at 11.5 s, for the second excitation. The purpose of this was to provide a clear visualization of the controller's effect on the system response. An example of such a response is illustrated in Figure 6.1, where the disturbance was defined as a 2.5 Hz sine wave with an amplitude of .02 m and a period of .4 s. From these plots, it is clear that the controller significantly increases the decay rate of all the AMD-1 responses.

Further improvements to the system's response were obtained by redesigning the feedback gain with the eigenvalue assignment and the LQR methods. Three sets of tests were considered, each utilizing a different set of parameter values: the original approximations, the Simulink toolbox estimations, and the sensor data calculations, which are documented in Table
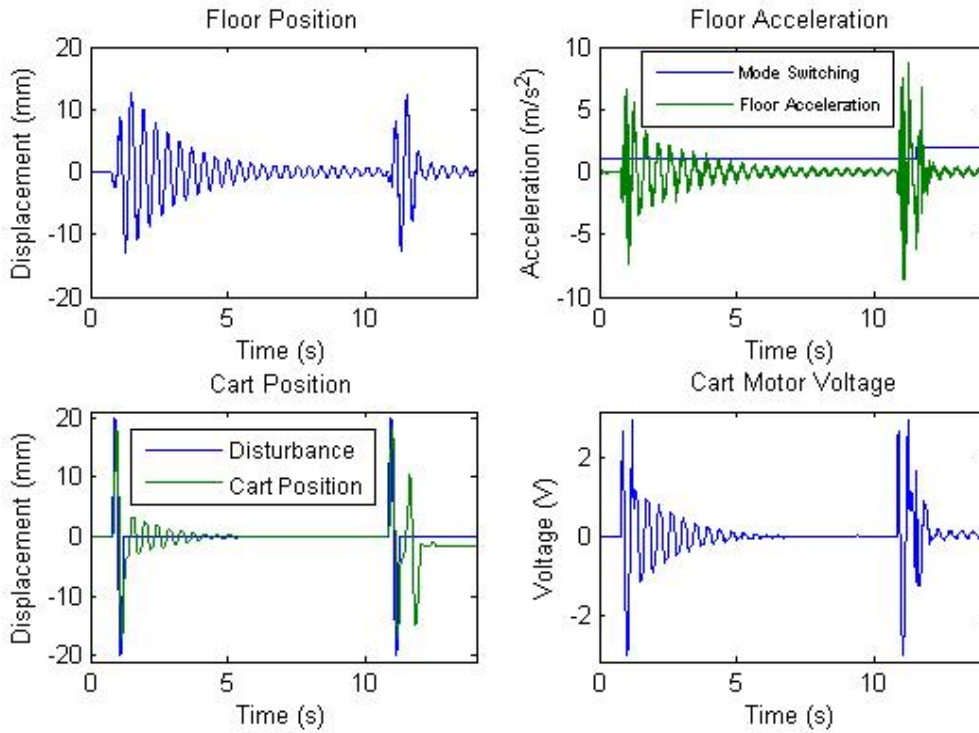
FIGURE 6.1: Floor position and acceleration, cart position, and cart motor voltage responses.

6.1. The corresponding gains for each set were determined and applied to the system, where simulated and experimental tests were analyzed.

TABLE 6.1: The Sets of System Parameters Values Used for Testing

System Parameters	Floor Mass M_f (kg)	Structure Damping B_f (Ns/m)	Floor Stiffness K_f (N/m)
Original Approximations:	1.3800	0.0000	500.9000
Simulink Estimations:	2.5090	3.2830	511.6000
Sensor Calculations:	1.6744	1.8898	470.0763

6.2 Estimated vs. Original Parameter Tests

To test the validity of the Simulink parameter estimations, their responses were compared to those of the original parameters. Figure 6.2 illustrates the floor position and cart motor voltage responses from both tests, superimposed onto one another. This comparison shows that

both sets of parameters seem to produce similar responses, but the estimated parameter test does appear have a slightly wider range of fluctuation.
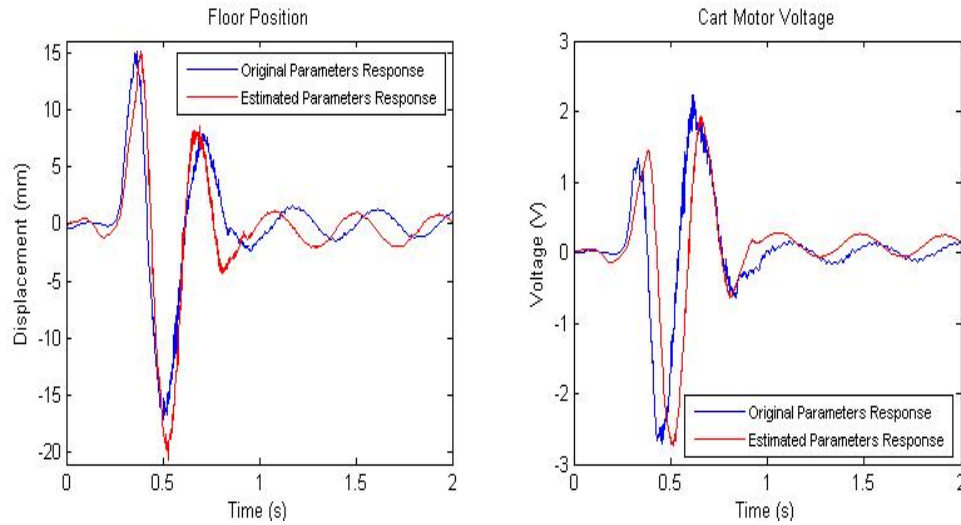
FIGURE 6.2: A comparison of the floor position (left) and cart motor voltage (right) data obtained from the original vs. estimated parameters.

To further analyze this comparison, the RMS values were calculated for each response. These values are displayed in Table 6.2, where it is observed that, for both the floor position and cart motor voltage results, the RMS values were smaller for the results obtained from the original parameter test. Furthermore, since the estimated parameter tests showed no improvement in the system response, further use of them was concluded to be unnecessary.

TABLE 6.2: RMS Values of the Original and Estimated Parameter Test Responses

Parameters	Floor Position RMS	Cart Motor Voltage RMS
Original	3.2197	0.4987
Estimated	3.5818	0.5017

6.3 Eigenvalue Assignment Results

The first method used to redesign the feedback control was the eigenvalue assignment method. This method improves the system response by focusing on increasing the response's

peak ratio reduction. As previously stated, the control theory says that this is done by moving the location of the system's dominant poles further to the left in the complex plane, where the dominant poles are the ones that produce the exponential function with the slowest decay rate. Recall, the AMD-1 system's pole locations, represented by: $\mathbf{P} = [-6 + 15j, -6 - 15j, -8, -16]$. Figure 6.3 illustrates the exponential functions produced by the real poles, -8 and -16, and the real part of the complex poles, -6. From this plot, it is evident that the dominant poles are "-6 ± 15".
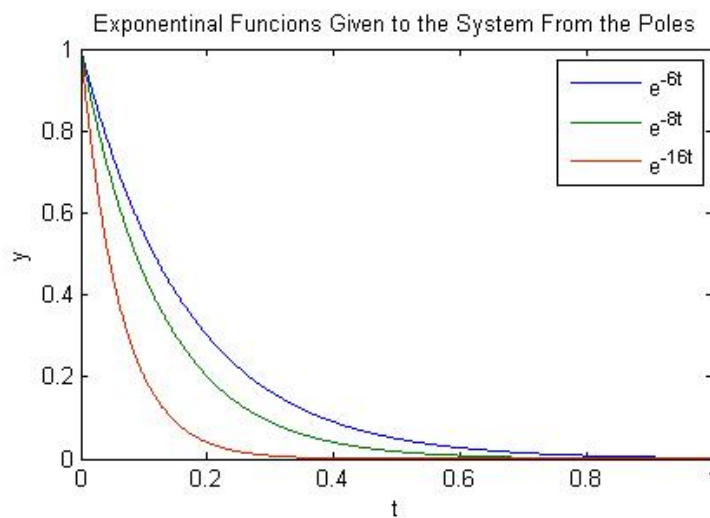
FIGURE 6.3: A plot of the exponential function provided by the closed-loop poles.

Due to certain constraints, the range for which these roots can be varied is limited. The lower variation limit is determined by the stability boundary, which is defined by the imaginary (or vertical) axis of the complex plane. The upper variation limit is determined by Earthly limitations, such as the availability of voltage, money, and resources. Figure 6.4 illustrates the location of each set of poles considered for the eigenvalue assignment tests.

Investigation into the effect the pole location has on the feedback design, and the effect the gain has on the AMD-1 system response, was analyzed through two sets of simulated and experimental tests. One test modeled the system with the original parameters and the other used the parameters calculated from the sensor tests. To update the plant and control system with the appropriate parameters and modifications, the MATLAB script 'EIGENVALUE.m,' found
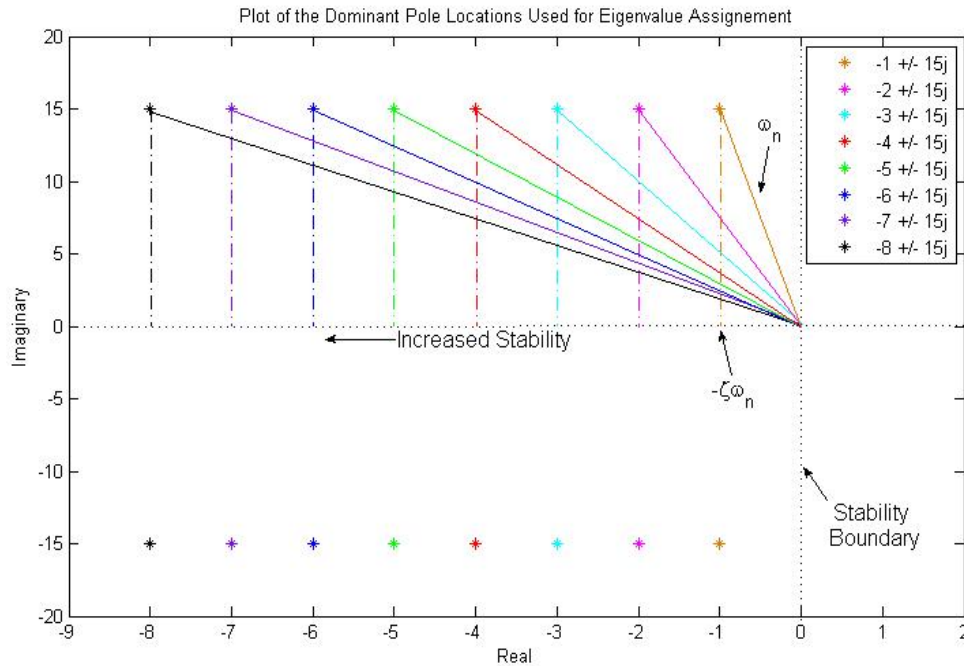
FIGURE 6.4: Location of the poles considered for the eigenvalue assignment tests.

in Appendix B, was used. Simulated data was obtained from the observer Simulink model in Figure D.1, and the experimental data was obtained from the experimental Simulink model with the Quarc software in Figure D.2. In the experimental Simulink diagram, the excitation mode was re-programed to last from 0 s to 1.5 s, with the disturbance starting at .8 s and ending at 1.2 s, and the damping mode was re-programmed to last from 1.5 s to 5 s.

The primary goal of this test is to increase the decay rate of the structure by minimizing the floor acceleration output. For that reason, the peak heights were measured and the RMS values were calculated from this output's response. Note, for the experimental responses, all data was gathered after 1.5 s, when the controller was turned on. This corresponding resultant peak and RMS data is organized into Table 6.3

When studying this table, is observed that the heights seem to decrease as the dominant poles increase. Also, notice this decrease in peak heights is directly related to the increase in value of the feedback gains. For further analysis, these peak heights were plotted to illustrate the actual trends. The simulated and experimental peak trend plots for each parameter test are

TABLE 6.3: Eigenvalue Assignment Results: Experimental and Simulated Floor Acceleration Peak and RMS Data

Original Parameters: $M_f = 1.38$ kg, $B_f = 0$ Ns/m, $K_f = 500.9$ N/m							
				$\ddot{x}_f$ Peak Height		$\ddot{x}_f$ RMS Data	
Pole	Feedback Gain **K**			Simulated	Experimental	Simulated	Experimental
				(m)	(mm)	(m)	(mm)
-1	[39.0474	53.3504	1.4436	-3.0995]	0.4577	3.5690	0.1929	1.0896
-2	[39.5657	1.9216	1.8863	-3.7971]	0.4315	3.7840	0.1887	0.8373
-3	[40.4296	-50.5084	2.3939	-4.2923]	0.4067	4.910	0.1882	0.7696
-4	[41.6390	-103.9395	2.9662	-4.5852]	0.3841	6.2750	0.1881	0.7772
-5	[43.1940	-158.3717	3.6033	-4.6758]	0.3640	5.6280	0.1860	0.7157
-6	[45.0945	-213.8050	4.3052	-4.5640]	0.3485	5.6520	0.1858	0.7002
-7	[47.3406	-270.2395	5.0719	-4.2498]	0.3355	4.8860	0.1869	0.7406
-8	[49.9323	-327.6750	5.9034	-3.7333]	0.3242	4.3110	0.1855	0.7056

Sensor Parameters: $M_f = 1.6744$ kg, $B_f = 1.8898$ Ns/m, $K_f = 470.0763$ N/m							
				$\ddot{x}_f$ Peak Height		$\ddot{x}_f$ RMS Data	
Pole	Feedback Gain **K**			Simulated	Experimental	Simulated	Experimental
				(m)	(mm)	(m)	(mm)
-1	[38.7942	50.9969	2.9150	2.3436]	0.5003	3.066	0.2061	1.4621
-2	[39.3092	5.1399	3.3520	1.9665]	0.4675	3.9760	0.2029	0.9905
-3	[40.1674	-41.1770	3.8515	1.8129]	0.4373	3.8320	0.2010	0.8446
-4	[41.3690	-87.9538	4.4134	1.8826]	0.4105	4.5990	0.2010	0.8203
-5	[42.9139	-135.1906	5.0377	2.1756]	0.3877	4.5510	0.1988	0.8109
-6	[44.8021	-182.8873	5.7246	2.6919]	0.3724	6.1790	0.1989	0.8243
-7	[47.0337	-231.0440	6.4738	3.4316]	0.3599	4.4070	0.2005	0.8062
-8	[49.6085	-279.6606	7.2856	4.3946]	0.3475	6.3470	0.1989	0.8495

illustrated in Figure 6.5. Analysis of these trends indicate that there are discrepancies between the simulated and experimental trends. The simulated trends for both sets of parameter tests produced a desirable peak trend, where the peak heights decrease as the poles moved further from the stability boundary. The experimental trends, on the other hand, produced inconsistent and undesirable trends. Investigation into the reason for this discrepancy will be discussed later, but first, analysis of the RMS trends will be considered.

The RMS value trends were also plotted and are illustrated in Figure 6.6. Analysis of these trends indicate that both parameter tests produced experimental RMS trends that closely represent the simulated RMS trends. It is also observed that these RMS trends reveal an acceptable, decreasing tendency, with the exception of one (or two) stray RMS values that produced a peak(s) in the curve. These peaks could be an effect of improper testing procedure or data collection. They could also be a result of the system's physical constraints, such as, the voltage

FIGURE 6.5: Eigenvalue Assignment Results: Simulated and experimental floor acceleration peak trends, for both parameter tests.

supply and controller capability.

Next, investigation into reason for the discrepancies found in the experimental peak trends was considered. First, two of the floor acceleration responses were superimposed onto one another to visualize the effect that the pole location had on the output's decay rate. The responses that were chosen for comparison were obtained from the tests where the dominant poles where at '−6' and '−3.' This comparison is illustrated in Figure 6.7, for the original parameter tests, and in Figure 6.8 for the sensor parameter parameter tests.

Both plots reveal that there is a great deal of noise present in the floor acceleration data, which interferes with accurate data collection of its peak heights. Even so, in both cases, it can still be recognized that the smaller pole, −6, produced a response that decayed quicker. Nevertheless, to obtain better peak analysis results, two alternate processes were considered: the use of the floor position responses to obtain peak height data and the addition of a filter in the state observer to reduce the the effect of noise.
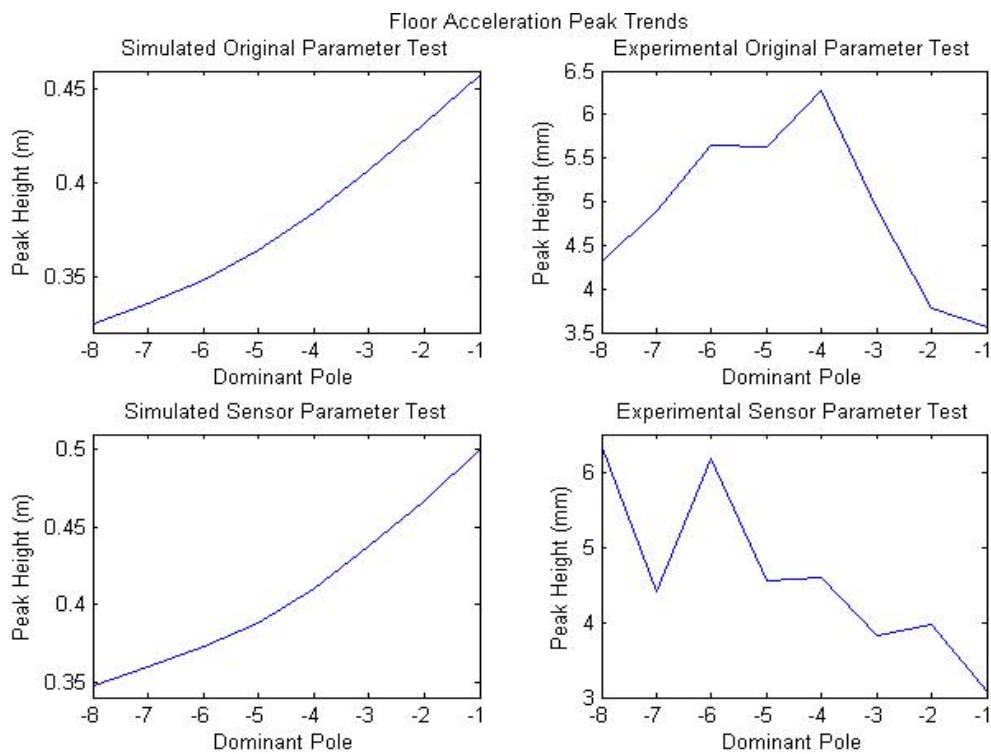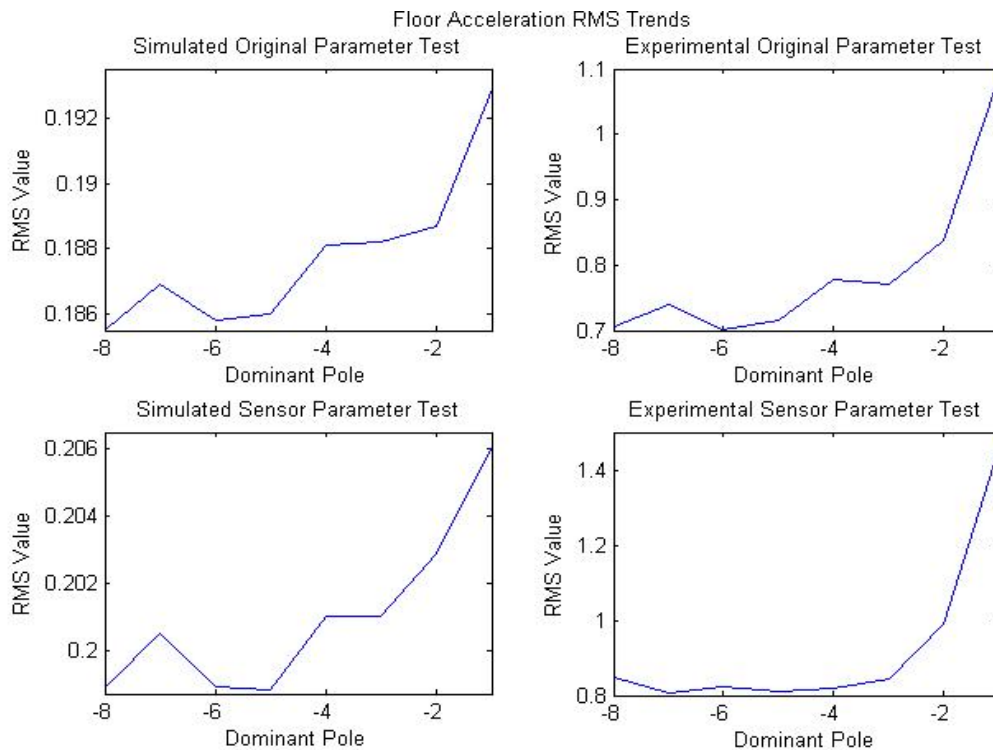
FIGURE 6.6: Eigenvalue Assignment Results: Simulated and experimental floor acceleration RMS trends, for both parameter tests.

When the floor position data was used to measure the heights, the first three peaks were considered, again after 1.5s. These heights were used to calculate and compare the response's peak ratio reduction over time. These peak heights and the ratios of 'peak one to peak two' and 'peak two to peak three' are documented in Table 6.4. Notice that, for both parameter tests, the peak heights decrease more significantly when smaller poles are used, which wass verified by the peak ratio values.

A larger peak ratio value indicates the presence of a quicker decay rate. From the table's values, it is revealed that the ratios increase as the poles decrease. This is verification that the smaller poles produce the more desirable responses. Also, from this table, it is concluded that the original parameter results produced better results than the sensor parameters. However, this is not to say that the sensor parameters are bad. Recall, the original parameter neglected the damping coefficient of the structure; therefore, the sensor parameters actually produce a more accurate AMD-1 response.
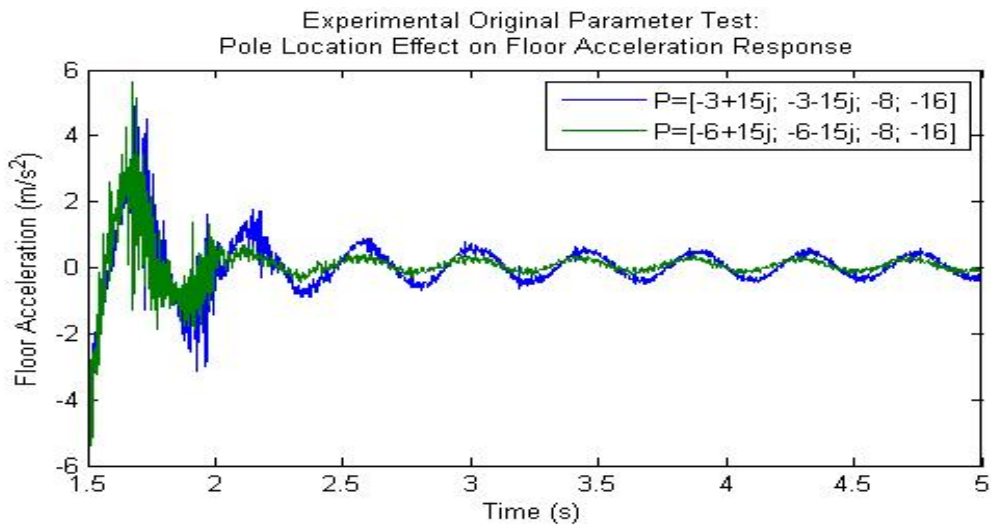
FIGURE 6.7: Eigenvalue Assignment Results: Original parameter floor acceleration responses, produced when the controller's dominant pole locations were at -3 and -6.
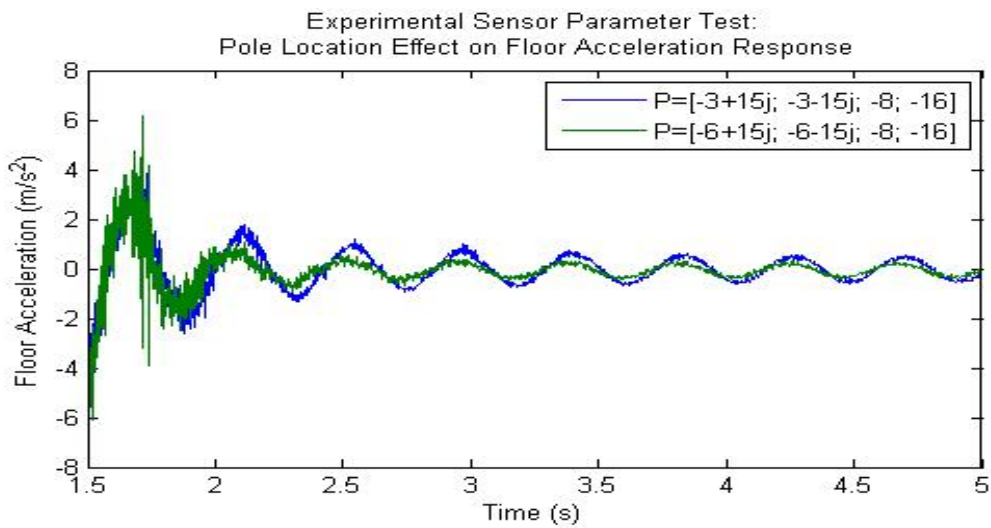
FIGURE 6.8: Eigenvalue Assignment Results: Sensor parameter floor acceleration responses, produced when the controller's dominant pole locations were at -3 and -6.

Next, a filter was applied to the state observer, which produced clearer floor acceleration responses with considerably less noise discrepancy. Just as before, the RMS values were computed, and the peak heights were measured, for the new filtered floor acceleration responses. However, this time the heights were measured from the data produced after 1.5 s (when the damper was turned on) and the first four peaks were considered. Additionally, the first five

TABLE 6.4: Eigenvalue Assignment Results: Floor Position Peak Ratio Data From Both Parameter Tests

	Original Parameters: $M_f = 1.38$ kg, $B_f = 0$ Ns/m, $K_f = 500.9$ N/m					Sensor Parameters: $M_f = 1.38$ kg, $b = 0$ Ns/m, $K_f = 500.9$ N/m				
	Peak Height (mm)			Peak Ratio		Peak Height (mm)			Peak Ratio	
Pole	Pk1	Pk2	Pk3	Pk1/Pk2	Pk2/Pk3	Pk1	Pk2	Pk3	Pk1/Pk2	Pk2/Pk3
-1	12.01	9.532	7.4390	1.2600	1.2814	14.76	11.820	10.320	1.2487	1.1453
-2	11.92	7.922	4.8130	1.5047	1.6460	14.90	9.620	6.653	1.5489	1.4460
-3	11.23	6.222	2.8730	1.8049	2.1657	14.54	7.771	4.767	1.8710	1.6302
-4	11.28	5.079	1.9010	2.2209	2.6718	14.59	6.878	3.325	2.1212	2.0686
-5	11.21	4.516	1.6460	2.4823	2.7436	14.16	5.826	2.772	2.4305	2.1017
-6	10.72	3.437	0.8479	3.1190	4.0535	13.88	5.249	2.349	2.6443	2.2346
-7	11.21	3.270	1.1210	3.4281	2.9170	13.93				
-8	10.91	2.825	0.8032	3.8619	3.5172	13.02				

peak heights of the corresponding input voltage data were also collected to gain a better understanding of how the excitation and controller effect the floor acceleration response.

The filtered floor acceleration and voltage peak heights, measured from the original and sensor parameter test, are documented in Table 6.5. Just by comparing the table's acceleration data values, it is observed that the floor acceleration's first peak varies for each pole, but the proceeding peaks decrease the fastest for the smaller poles. The table's voltage data, on the other hand, was found to be a little more difficult to analyze. For this reason, a better visualization of these trends was obtained by plotting their values.

TABLE 6.5: Eigenvalue Assignment Results: Experimental Voltage and Filtered Floor Acceleration Peak Data

Original Parameters: $M_f = 1.38$ kg, $B_f = 0$ Ns/m, $K_f = 500.9$ N/m									
	V_m Peak Data (V)					$\ddot{x}_f$ Peak Data (mm), After 1.5 s			
Pole	Pk1	Pk2	Pk3	Pk4	Pk5	Pk1	Pk2	Pk3	Pk4
	(.8 s)	(1.2 s)	(1.502 s)	(1.8 s)	(2.2 s)				
-1	2.735	2.989	-0.9482	0.9277	0.7047	2.465	1.8450	1.4790	1.2540
-2	2.752	2.992	-0.3879	0.8559	0.4475	2.618	1.5090	1.0570	0.8677
-3	2.750	3.000	0.0809	0.8555	0.2850	2.395	0.9670	0.6626	0.4492
-4	2.779	2.978	0.6189	0.9224	0.2254	2.411	0.7826	0.5409	0.4382
-5	2.594	2.983	1.1300	0.9453	0.2173	2.348	0.6074	0.3691	0.3076
-6	2.782	2.971	1.6250	1.0060	0.2036	2.347	0.3997	0.2980	0.2748
-7	2.755	2.991	2.1490	1.0440	0.2141	2.364	0.2927	0.2035	0.1697
-8	2.774	2.951	2.6960	1.0350	0.2112	2.558	0.2501	0.1821	0.1501

Figure 6.9 illustrates a plot of the voltage data's peak trends that were produced from each eigenvalue assignment test. Recall, the disturbance was programmed to start at .8 s and end at 1.2 s. That being said, it can be speculated that the first two peaks are simply a result of the excitation, explaining why they are essentially the exact same for each eigenvalue assignment test. Also recall, the controller was programed to turn on at 1.5 s. This explains the peaks that crest at 1.502 s. Notice, that these peaks are quite small for the poles closest to the stability boundary, but they quickly increase as the poles decrease. Observation of the remaining peaks show that they again converge to approximately the same value. From these observations, it is found that the only difference in the voltage peak heights are an effect of the controller voltage. When compared to the floor acceleration peaks, the conclusion is, as increased stability is achieved, increased voltage is used. Therefore, for design purposes, this max voltage will need to be regulated because it is directly related to the cost of control.
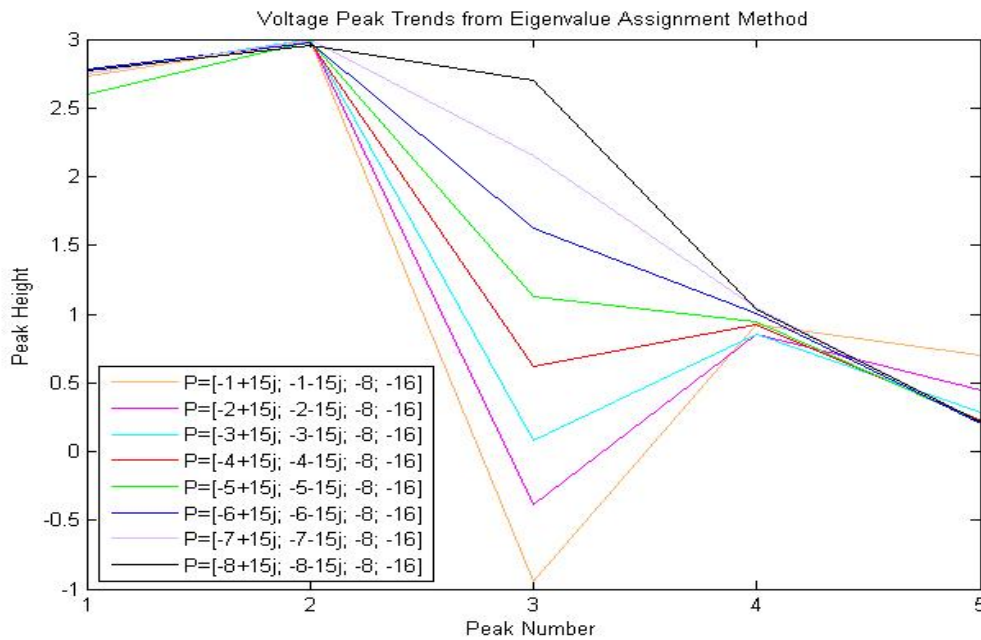

FIGURE 6.9: Eigenvalue Assignment Results: Voltage peak trends.

Next, the RMS values were used to analyze the filtered floor acceleration and corresponding voltage responses. This time, three cases were considered for the calculation of the RMS values: after 1.5 s (when the controller was turned on), after 1.502 s (when the maximum

TABLE 6.6: Eigenvalue Assignment Results: Experimental Filtered Floor Acceleration RMS Data

Original Parameters: $M_f = 1.38$ kg, $B_f = 0$ Ns/m, $K_f = 500.9$ N/m					
	V_m RMS Data			$\ddot{x}_f$ RMS Data	
Pole	1.5 s	1.502 s	1.6 s	1.5 s	1.502 s	1.6 s
-1	0.3881	0.3875	0.3594	1.0313	1.0297	1.0002
-2	0.2628	0.2618	0.2401	0.8012	0.7991	0.7554
-3	0.2299	0.2286	0.2108	0.6653	0.6625	0.5935
-4	0.2408	0.2398	0.2240	0.6109	0.6081	0.5247
-5	0.2618	0.2607	0.2401	0.5833	0.5803	0.4737
-6	0.2919	0.2910	0.2616	0.5709	0.5677	0.4450
-7	0.3182	0.3174	0.2771	0.5676	0.5643	0.4225
-8	0.3601	0.3594	0.3048	0.5872	0.5840	0.4189

voltage peaked) and 1.6 s (after the system has had time to react to the controller). Consideration of all these cases provided better understanding of how to interpret the RMS values. The collected RMS values, for the voltage and filtered floor acceleration responses, are organized into Table 6.6. Relatively speaking, both sets of RMS calculated after 1.5 s and 1.502 s seem to be about the same, which is expected since they are only separated by .002 s. Looking at the voltage RMS values, the trend looks like it decreases but then increases after a certain point. However, the filtered floor acceleration RMS values seem to have a steadily decreasing trend about them. Nonetheless, both sets of values will be plotted for a clearer visualization of their trend.

Figure 6.10 illustrates plot of the voltage RMS trends obtained from each case. Notice how the voltage RMS trends decrease from pole -1 to -3, and then proceed to increase. The trend's decreasing slope is due to the negative controller peaks (Peak 3 at 1.502 s) for poles -1 and -2. Even though these larger poles designed a controller that used a minuscule amount of voltage, their output results has a much slower decay rate than the smaller poles. Furthermore, the remaining increase in the voltage trends indicate that an increased amount of voltage is required when smaller poles are used to design the feedback control.

Figure 6.11 illustrates the filtered floor acceleration RMS trends, obtained from each case. It is observed that the trend has a decreasing slope. Notice, for the RMS values that
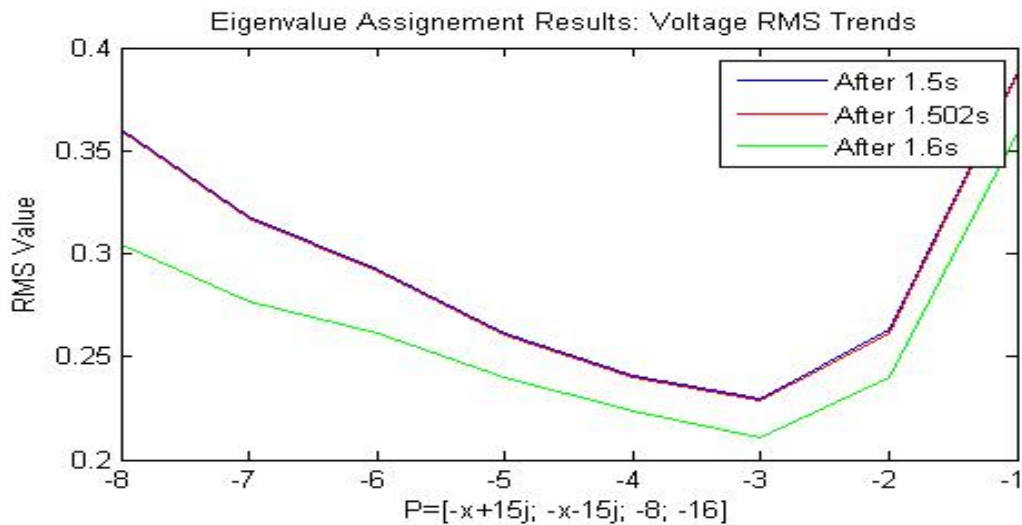
FIGURE 6.10: Eigenvalue Assignment Results: Voltage RMS trends.

were obtained after 1.5 s and 1.502 s, there exists a slight increase in the trend produced by the smaller poles, which could be and effect of the controller. However, when the RMS values were calculated after 1.6 s, this increasing effect no longer exists.
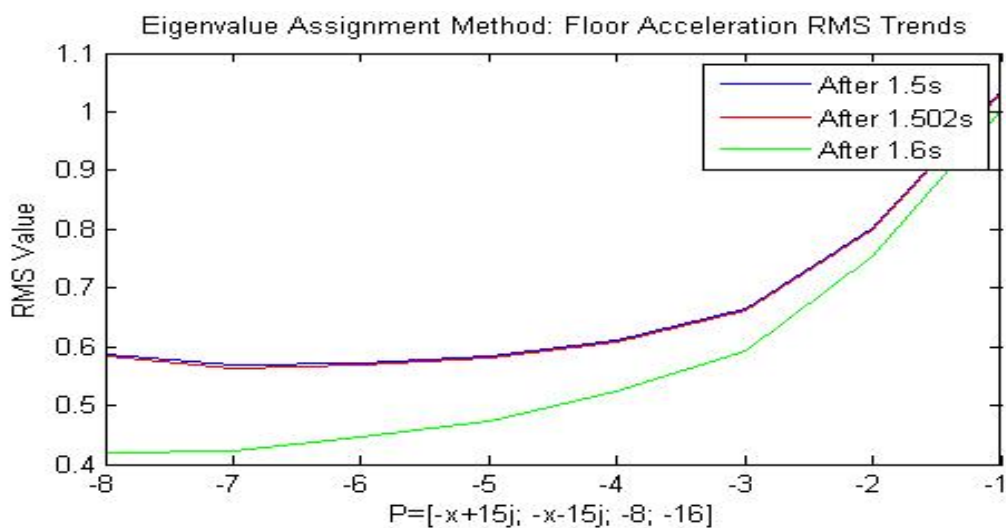
FIGURE 6.11: Eigenvalue Assignment Results: Filtered floor acceleration RMS trends.

In conclusion to these eigenvalue assignment tests, it was found that increased stability is achieved by designing the feedback controller with smaller poles. It was also found that as increased stability is achieved, a higher controller voltage is required. Therefore, the optimal

feedback design is achieved by using the smallest pole possible that keeps the required voltage within the allowable range. In the end, more money means more voltage, which leads to improved controller and output performance.

6.4   Linear Quadratic Regulation

The other method used for feedback design was the Linear Quadratic Regulation method. This method balances the importance of the system's control effort, V_m, and the system's error, $V_m - Y$. Recall from the background section that this is done by adjusting the values of the input weight matrix, **R**, and the output weight matrix, **Q**, while being mindful of the limitation for each.

Consideration for both limitations leaves only a select range of possible **R** and **Q** values. Since there is only one input to the system, the value for **R** remains a single constant. For these LQR tests, the considered values ranged from 1 to .001, decreasing by a power of tent. Since the AMD-1 system has four states, **Q** must be defined by a 4×4 matrix; therefore, **Q** was initially defined by the 4×4 identity matrix. Reacall, as a value of **Q** is increased, more effort is put into reducing the state variable that corresponds to that value. Since the main focus of the feedback design is to reduce the floor's oscillation, the value of Q(2,2), which represents the floor's position, was chosen to be increased because it is directly related to the floor acceleration. The rang of values considered for Q(2,2) were: 1, 5, 20, 50, and 100.

For all the simulated and experimental LQR tests, the control system was updated with the MATLAB code 'LQR.m' in Appendix C, where the different values of **R** and **Q** were used to design different feedback gains. Many simulations were run to gain an understanding of the effect **R** and **Q** had on the system response. Observations suggested that decreasing **R** reduced the floor's oscillation, and increasing **Q** eliminated the floor's oscillation, while also reducing the peak heights. The LQR-designed controller was then tested on the AMD-1 system and analyzed by comparing the RMS values that were obtained from the

filtered floor acceleration data and corresponding voltage data, after 1.6s, since those criteria produced the best results for the eigenvalue assignment tests.

The calculated RMS data pertaining to the filtered floor acceleration responses is organized into Table 6.7, and that of the voltage responses is organized into Table 6.8. Here, the left column of both tables represents the different **Q** values considered for testing, and the considered **R** values are represented in the rows under the parameters. Notice that the filtered floor acceleration RMS values seem to decrease as **Q** increases and **R** decreases. On the contrary, the voltage RMS values seem to increase as **Q** increases and **R** decreases. Again, these values were plotted to provide a visual representation of the RMS trends based on the input and output weight functions used to design the feedback control.

TABLE 6.7: LQR Results: Experimental Filtered Floor Acceleration RMS Data

Original Parameters: $M_f = 1.38$ kg, $B_f = 0$ Ns/m, $K_f = 500.9$ N/m				
Q \R	1	0.1	0.01	0.001
Identity	0.7648	0.7181	0.6499	0.5822
5	0.7615	0.7327	0.6364	0.5818
20	0.7784	0.7428	0.6468	0.5891
50	0.7524	0.7197	0.6122	0.5625
100	0.7595	0.7004	0.6038	0.5343

TABLE 6.8: LQR Results: Experimental Voltage RMS Data

Original Parameters: $M_f = 1.38$ kg, $B_f = 0$ Ns/m, $K_f = 500.9$ N/m				
Q \R	1	0.1	0.01	0.001
Identity	0.0070	0.0449	0.1392	0.1833
5	0.0069	0.0454	0.1394	0.1833
20	0.0068	0.0467	0.1436	0.1866
50	0.0076	0.0503	0.1447	0.1878
100	0.0086	0.0528	0.1499	0.1926

Figure 6.12 illustrates the the trend of the filtered floor acceleration responses RMS values with respect to **R**, and each trend represents a different **Q** value. These trends show that as **R** decreases, so does the RMS value. Meaning, the smaller input weights produce responses with increased decay rates. Also, the RMS values decrease more rapidly as **R** decreases when larger values of **Q** are used. Therefore, the best output response is achieved with smaller **R** values and larger **Q** values. However, there is limit to how small the input, and how large the output, weights can be made.

Figure 6.13 represents the the voltage response's RMS trend, plotted on the same axes as the filtered floor acceleration. These trends indicate that more voltage is required when **R** is
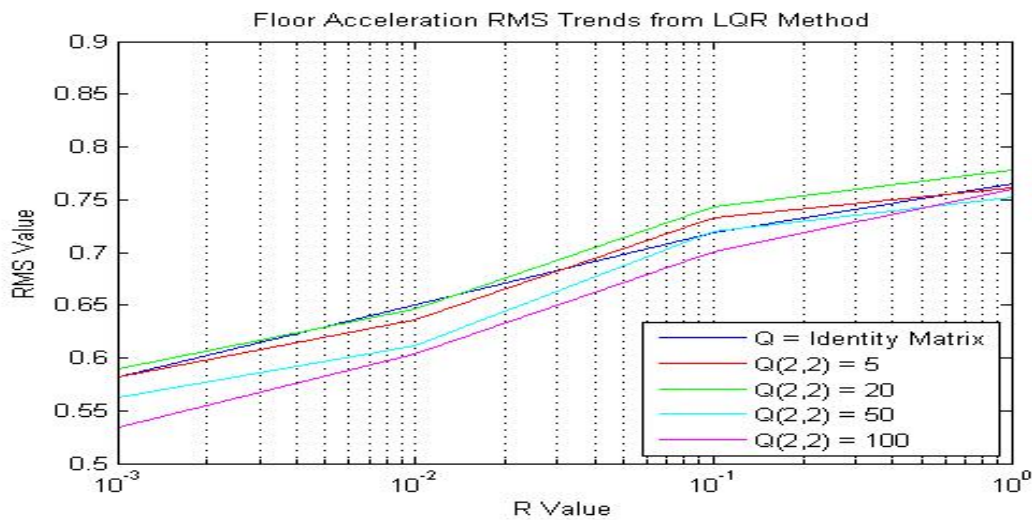
FIGURE 6.12: LQR results: Filterend floor acceleration RMS trends.

smaller. It is also observed that as **Q** is increased, the RMS values increase more rapidly as **R** decreases.
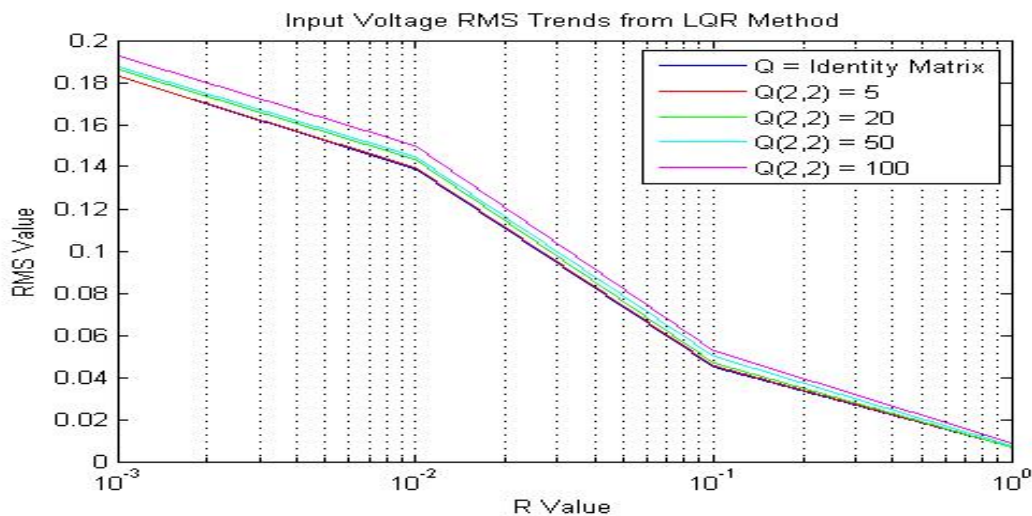
FIGURE 6.13: LQR results: Voltage RMS trends.

Furthermore, these LQR results support the conclusion that larger **Q**'s and smaller **R**'s are used to design a contoller that decays the system the fastest, but requires the most voltage. Just the same, when the system's requirements and the resources available are known, an optimal feedback controller can be designed by balancing the importance of the input with the importance of the system's output.

CHAPTER 7

CONCLUSION

This work presents an effective method for deriving the AMD-1 EOM, an improved model of the AMD-1 system, and the design of a feedback control that successfully reduces the oscillation of the AMD-1 structure upon excitation. The new derivation of the EOM used the system's free body diagram and its results were validated with Quanser's EOM, which was obtained from the Lagrange's Method. This model was improved by considering the effect of the structure's viscous damping. The value of this damping coefficient, along with the corresponding floor's stiffness and mass, was determined through the force and motion sensor data analysis.

Furthermore, two feedback design techniques were applied: eigenvalue assignment and LQR. Analysis of both techniques were used to determine which method was more appropriate and efficient. It was concluded that when the output's primary focus is to satisfy the time-domain specifications, then the eigenvalue assignment method is more effective. When the output's focus is to balance the importance of the control effort with the importance of reduced vibration, then the LQR method becomes more effective.

7.1 Discussion

Simulated eigenvalue results indicated that the optimal floor acceleration responses were obtained when the system's feedback control was designed with the dominant pole's that were further from the stability boundary in the complex plane. However, the experimental results, showed that little, to no, improvement was achieved once the poles moved past a certain point. Comparison of the corresponding voltage responses showed that the demand for more power increased more drastically as the dominant poles surpassed -6.

The LQR results indicated that the optimal response was achieved when $\mathbf{Q}(2,2) = 100$ and $\mathbf{R} = .001$, in other words, when $\mathbf{Q}$ was larger and $\mathbf{R}$ was smaller. This conclusion was made from the RMS value trend analysis. Also, despite the fact that these $\mathbf{Q}$ and $\mathbf{R}$ values required the highest amount of voltage out of all the LQR tests, comparison showed that there was no alarming significance in the required voltage.

Furthermore, even though the feedback control that was designed in this work was made specific to an AMD system, it could be applicable in any structure susceptible to wind or ground excitation. As research continues, the efficiency and credibility of such a control system is sure to grow, increasing the potential to save lives and preserve structures.

7.2   Future Research

Future research in this field could focus on the compensation for the presented system's limitations, or the derivation of a model that would reduce modeling error. Any time an assumption is made, it increases the potential for error. When deriving the mathematical model of the AMD-1 system, many parameters were neglected, or assumed to be negligible. Recall, the nonlinear coulomb friction applied to the linear cart, the viscous damping force applied to the floor, the friction between the cart and the structure, and the natural structure damping were all neglected. In addition, the gravitational potential energy was assumed to be negligible. Future research could develop a method that would include the loss due to these parameters or verify their negligence.

With respect to resource availability, the accessibility to a larger power source and/or higher accuracy amplifiers and sensors would guarantee the achievement of a higher degree of stability. In addition, a method that would accurately estimate the system parameters (mass, spring constant and damping coefficient) could be proposed, which would result in a even more accurate model of the system.

It should also be considered that, in reality, the buildings and structures at the highest risk have multiple degrees of freedom and their system parameters continually fluctuate over time. A structure's mass fluctuates daily as an effect of various personnel and merchandise continually entering and leaving, and a structure's stiffness and viscous damping fluctuates over the years as an effect of aging and weathering. Therefore, some other ideal topics of study would include the modeling of MIMO systems and the addition of an adaptation system that would continuously estimate the system parameters and update the control system.

REFERENCES

[1] 4.5+ Magnitude Earthquakes since 1973. (n.d.). *Google Fusion Tables*. Retrieved March 4, 2014, from https://www.google.com/fusiontables/DataSource?dsrcid=579510.

[2] Agrawal, A. K., Yang, J. N., Schmitendorf, W. E., & Jabbari, F. (1997). Stability of Actively Controlled Structures with Actuator Saturation. *Journal of Structural Engineering, 123*(4), 505.

[3] Alkhatib, R., & Golnaraghi, M. F. (2003). Active Structural Vibration Control: A Review. *The Shock and Vibration Digest, 35*(5), 367-383.

[4] Ashokkumar, C. R., & Iyengar, N. (2011). Partial Eigenvalue Assignment for Structural Damage Mitigation. *Journal of Sound and Vibration, 330*(1), 9-16.

[5] Bdar, S., Prof. Shuyan, M., Saifullah, S., & Dr. Jie, H. (2013). Comparison of PID, Pole Placement and LQR Controllers for Speed Ratio Control of Continuously Variable Transmission (CVT). *ICAMECE 2013*, 149-153.

[6] Ding, Y. C., Weng, F. L., & Yu, Z. A. (2013). Actuator Saturation and Control Design for Buildings Structural Systems with Improved Uncertainty Description. *Shock and Vibration, 20*(2), 297-308.

[7] Gajic, Z., & Lelic, M. (1996). Chapter 5: Controllability and Observability. *Modern Control Systems Engineering*. London: Prentice Hall.

[8] Guzzardo, C. A., (2012). *Optimal Actuation in Active Vibration Control using Pole-Placement*. (Unpublished doctoral dissertation). Louisiana State University and Agricultural and Mechanical College, Louisiana.

[9] Hanagan, L. M., & Murray, T. M. (1997). Active Control Approach for Reducing Floor Vibrations. *Journal of Structural Engineering, 123*(11), 1497–1505.

[10] Hanagan, L. M., Kulasekere, E. C., Walgama, K. S., & Premaratne, K. (2000). Optimal Placement of Actuators and Sensors for Floor Vibration Control. *Journal of Structural Engineering, 126*(12), 1380-1387.

[11] Hochrainer, M. J. (2005). Tuned Liquid Column Damper for Structural Control. *Acta Mechanica, 175*(1-4),57-76.

[12] Juang, J., & Maghami, P. G. (1990). Robust Eigensystem Assignment for Second-Order Dynamic Systems. *Mechanics and control of Large Flexible Structure, Progress in Astronautics and Aeronautics, 129*(14), 373-387.

[13] Junkins, J. L., & Kim, Y. (1990). Minimum Sensitivity Design Method for Output Feedback. *Mechanics and Control of Large Flexible Structure, Progress in Astronautics and Aeronautics, 129*(15), 389-409.

[14] Kumar, R., & Khan, M. (2007). Pole Placement Techniques for Active Vibration Control of Smart Structures: A Feasibility Study. *Journal of Vibration and Acoustics, 129*(5), 601-615.

[15] Landau, I. D., Lozano, R., M'Saad, M., & Karimi, A. (2011). *Adaptive control algorithms, analysis and applications* (2nd ed.). London: Springer.

[16] Lin, Y. K., & Yong, Y. (1987). Evolutionary Kanai-Tajimi Type Earthquake Models. *Journal of Engineering Mechanics, 113*(8).

[17] Luca, S. G, Chira, F., & Rosca, V. O. (2005). Passive, Active and Semi-Active Control Systems in Civil Engineering. *Tomul LI (LV), Fasc. 3*(4) 23-31.

[18] Manufacturing Education 1998. *Free decay curve*. [Plot]. Retrieved from http://www.mfg.mtu.edu/marc/primers/machtool/vibration/damping.html

[19] Marinova, D., & Marinov, V. (2005). Numerical Design of Optimal Active Control for Seismically-Excited Building Structures. *Numerical Analysis and Its Applications: Third*

International Conference, NAA 2004, Rousse, Bulgaria, June 29-July 3, 2004: Revised Selected Papers, Berlin: Springer, 408-415.

[20] Maurer Sohnoe - Innovation in Steel. (Since, 1876). Maurer Tuned Mass Dampers - Technical Information and Products. Retrieved May. 19, 2014,

[21] Meadows, H. E. (2006). Controllability and Observability in Time-Variable Linear Systems. *SIAM Journal on Control, 5*, 64-73.

[22] Munich Re. n.d. *Leading natural disasters, by overall economic losses, since 1980*. [Map]. Retrieved from http://www.economist.com/node/21542755

[23] Mei, G., Kareem, A., & Kantor, J. C. (2001). Real-Time Model Predictive Control of Structures under Earthquakes. *Earthquake Engineering & Structural Dynamics, 30*(7), 995-1019.

[24] Mei, G., Kareem, A., & Kantor, J. C. (2002). Model Predictive Control of Structures Under Earthquakes using Acceleration Feedback. *Journal of Engineering Mechanics, 128*(5), 574.

[25] No Author. Linear-Quadratic Regulator (LQR) Design. (2014, January 1). Retrieved June 2, 2014, from http://www.mathworks.com

[26] No Last Name, James. 2011. *Worldwide map of nuclear power stations and earthquake zones*. [Map]. Retrieved from http://maptd.com/worldwide-map-of-nuclear-power-stations-and-earthquake-zones/

[27] Nuclear Power Stations Worldwide. (n.d.). *Google Fusion Tables*. Retrieved March 4, 2014, from https://www.google.com/fusiontables/DataSource?dsrcid=579353

[28] Ouyang, H., & Singh, K. V. (2010). Pole Assignment for Asymmetric Systems Using State- feedback with Time Delay. *Active Vibration Control, Proceedings of ISMA2010 Including USD2010*, 383-390.

[29] Quanser. Active Mass Damper - One Floor. *Linear Experiment #9: Vibration control*, 1-19.

[30] Robinson, J. K., Gamble, S. L., & Myslimaj, B. M. (2007, June) Supplemental Damping and Using Tuned Sloshing Dampers. *STRUCTURE Magazine: Practical Solutions - Real World Solutions for the Practicing Structural Engineer*, 14-18.

[31] Sakai, H., & Arase, M. (1979). Recursive Parameter Estimation of an Autoregressive Process Disturbed by White Noise. *International Journal of Control, 30*(6), 949-966.

[32] Scheller, J., & Starossek, U. (2011). A versatile active mass damper for structural vibration control. *Proceedings of the 8th International Conference on Structural Dynamics, EURODYN 2011: Leuven, Belgium, 4-6 July 2011*, S.I: s.n.j., 1777-1784.

[33] Sivanadyan, T., & Sayeed, A. (2006). Active Wireless Sensing for Rapid Information Retrieval in Sensor Networks, *Information Processing in Sensor Networks, IPSN 2006. The Fifth International Conference*, 85-92.

[34] Slater, G. L., & Zhang, Q. (1990). Controller Design by Eigenspace Assignment. *Mechanics and Control of Large Flexible Structure, Progress in Astronautics and Aeronautics, 129*(17), 435-462.

[35] Tinkir, M., Kalyoncu, M., & Sahin, Y. (2013). Experimental Investigation of Full-Order Observer and LQR Controlled Building-Like Structure Under Seismic Excitation. *Applied Mechanics and Materials, 307*, 316-320.

[36] Watakabe, M., Chiba, O., & Kamada, T. (2004). Vibration Control of a Large-scale Test Building using Hybrid Mass Damper System Applied Robust Control Theory. *13th World Conference on Earthquake Engineering Vancouver, B.C., Canada August 1-6, 2004*.

[37] Willis, A. G., Bates, D., Fleming, A. J., Ninness, B., & Moheimani, S. O. (2008). Model Predictive Control Applied to Constraint Handling in Active Noise and Vibration Control. *IEEE Transactions on Control Systems Technology, 16*(1), 3-12.

[38] Yamamoto, M., Aizawa, S., Higashino, M., & Toyama, K. (2001). Practical Applications of Active Mass Dampers with Hydraulic Actuator. *Earthquake Engineering & Structural Dynamics, 30*(11), 1697-1717.

[39] Yamamoto, M., & Sone, T. (2013). Behavior of active mass damper (AMD) Installed in High-Rise Building During 2011 Earthquake off Pacific Coast of Tohoku and Verification of Regenerating System of AMD Based on Monitoring. *Structural Control and Health Monitoring*. 1.

[40] Zahrai, S.M., & Shafieezadeh, A. (2009). Semi-Active Control of the Wind-Excited Benchmark Tall Building using a Fuzzy Controller. *Iranian Journal of Science & Technology, Transaction B, Engineering, 33*(B1), 1-14.

APPENDIX A

MATLAB SCRIPT FOR SIMULATING THE AMD

```
     10pt
 1  %% Vm_SYSTEM.m
 2
 3  %% The system's physical constants were provided by Quanser's scripts
 4  %% The following scripts are used for modifications
 5
 6  %% PARAMETERS ————————————————————————————————————————————————
 7
 8  Mc=.65;          %Mass of cart (kg)
 9
10  %Original Approximations
11  Mf=1.38;         %Mass of floor (kg)
12  Bf=0;            %damping coefficient (Ns/m)
13  Kf=500.9;        %Spring constant of floor (N/m)
14
15  %Simulink Toolbox Estimations
16  % Mf=2.509;      %Mass of floor (kg)
17  % Bf=3.283;      %Damping coefficient (Ns/m)
18  % Kf=511.6;      %Spring constant of floor (N/m)
19
20  %Sensor Test Calculations
21  % Mf=1.6744;     %Mass of floor (kg)
22  % Bf=1.8898;     %Damping coefficient (Ns/m)
23  % Kf=470.0763;   %Spring constant of floor (N/m)
24
25  a=Kf/Mf;
26  M1=(Mc+Mf)/(Mc*Mf);
27  M2=-1/Mf;
28  K1=Kg^2*Kt*Km/Rm/r_mp^2;
29  K2=Kg*Kt/Rm/r_mp;
30
31
32  %% STATE VARIABLE REPRESENTATION ————————————————————————————
33  % Input = Vm
34  % Neglect Jm & Beq
35  % Eff_m = Eff_g = 1
36
37  A=[0 0 1 0;0 0 0 1;0 a -M1*K1 0;0 -a K1/Mf -Bf/Mf]; %System matrix
38  B=[0;0;M1*K2;-K2/Mf];                                %Input matrix
39  C=[1 0 0 0;0 -a K1/Mf -Bf/Mf];                       %Output matrix
40  D=[0;-K2/Mf];                                        %Input-output
41                                                       %matrix
42
43
```

```
44 %% SIMULATED SYSTEM ————————————————————————————————————
45
46 sys_Vm=ss(A,B,C,D);       %Steady state response
47
48
49 %% SIMULATION PLOTS ——————————————————————————————————————
50
51 figure(1)
52 step(sys_Vm)              %Step response
53
54 figure(2)
55 impulse(sys_Vm)           %Impulse response
56
57
58 %% CONTROLABILITY ——————————————————————————————————————
59 %The ability of an external input to modify the system states
60
61 CO=ctrb(A,B);             %Controllability matrix: CO=[B; AB; A^2B; A^3B]
62 rank(CO)                  %Controllable iff CN has full rank (rank=4)
63
64
65 %% OBSERVABILITY ————————————————————————————————————————
66 %The ability of the system outputs to interpret the system states
67
68 W=obsv(A,C);              %Observability matrix: W=[C; CA; CA^2; CA^3]
69 rank(W)                   %Observable iff W has full rank (rank=4)
70
71
72 %% POLE PLACEMENT DESIGN ————————————————————————————————
73
74 damp(A)                        %Open−loop poles
75 P=[−6+15j; −6−15j; −8; −16]; %Closed−loop poles
76                                %due to the state−feedback law
77
78 %% FULL−STATE FEEDBACK ——————————————————————————————————
79
80 figure(3)
81 K=place(A,B,P)                 %Full−state feedback gain Vector
82 AK=(A−B*K);                    %Stabilized system matrix
83
84
85 %% STABLIZED SYSTEM —————————————————————————————————————
86
87 sys_K=ss(AK,B,C,D);            %Stabilized system
88
89
90 %% SIMULATION PLOTS ——————————————————————————————————————
91
```

```matlab
92  figure(3)
93  step(sys_K)
94
95  figure(4)
96  impulse(sys_K)
97
98
99  %% FULL-ORDER OBSERBER ————————————————————————————————————————
100
101 OP=[−20; −25; −30; −35];        %Closed−loop poles
102                                 %due to the observer error dynamics
103 KO=place(A',C',OP);
104 G=KO';                          %Observer feedback gain matrix
```

APPENDIX B

MATLAB SCRIPT FOR EIGENVALUE ASSIGNEMENT

```
     10pt
 1 %% EIGENVALUE.m
 2
 3 %% VARIABLES ————————————————————————————
 4
 5 Mc=.65;          %Mass of cart (kg)
 6
 7 %Original Parameters
 8 Mf=1.38;         %Mass of floor (kg)
 9 Bf=0;            %damping coefficient (Ns/m)
10 Kf=500.9;        %Spring constant of floor (N/m)
11
12 %Simulink Toolbox Estimations
13 % Mf=2.509;      %Mass of floor (kg)
14 % Bf=3.283;      %Damping coefficient (Ns/m)
15 % Kf=511.6;      %Spring constant of floor (N/m)
16
17 %Sensor Test Calculations
18 % Mf=1.6744;     %Mass of floor (kg)
19 % Bf=1.8898;     %Damping coefficient (Ns/m)
20 % Kf=470.0763;   %Spring constant of floor (N/m)
21
22 a=Kf/Mf;
23 M1=(Mc+Mf)/(Mc*Mf);
24 M2=-1/Mf;
25 K1=Kg^2*Kt*Km/Rm/r_mp^2;
26 K2=Kg*Kt/Rm/r_mp;
27
28
29 %% STATE VARIABLE REPRESENTATION ————————————————
30 % Input = Vm
31 % Neglect Jm & Beq
32 % Eff_m = Eff_g = 1
33
34 A=[0 0 1 0;0 0 0 1;0 a -M1*K1 0;0 -a K1/Mf -Bf/Mf]; %System matrix
35 B=[0;0;M1*K2;-K2/Mf];                               %Input matrix
36 C=[1 0 0 0;0 -a K1/Mf -b/Mf];                       %Output matrix
37 D=[0;-K2/Mf];                                       %Input-output
38                                                     %matrix
39
40 %% POLE PLACEMENTS
       ————————————————————————————————
41
42 % P=[-1+15j; -1-15j; -8; -16];
```

```matlab
43  % P=[−2+15j ;  −2−15j ;  −8;  −16];
44  % P=[−3+15j ;  −3−15j ;  −8;  −16];
45  % P=[−4+15j ;  −4−15j ;  −8;  −16];
46  % P=[−5+15j ;  −5−15j ;  −8;  −16];
47  P=[−6+15j ;  −6−15j ;  −8;  −16];    %Original pole placements
48  % P=[−7+15j ;  −7−15j ;  −8;  −16];
49  % P=[−8+15j ;  −8−15j ;  −8;  −16];
50
51
52  %% STATE FEEDBACK GAIN ——————————————————————————————————————————————
53
54  K=place (A,B,P)
55
56
57  %% OBSERVER FEEDBACK GAIN ————————————————————————————————————————————
58
59  OP=[−20;  −25;  −30;  −35];
60  KO=place (A' ,C' ,OP) ;
61  G=KO' ;
```

APPENDIX C
MATLAB SCRIPT FOR LQR

10pt

```
 1 %% LQR.m
 2
 3 %% R & Q balance the importance of the control effort & error
 4
 5 %% VARIABLES ——————————————————————————————————
 6
 7 Mc=.65;          %Mass of cart (kg)
 8
 9 %Original Parameters
10 Mf=1.38;         %Mass of floor (kg)
11 b=0;             %damping coefficient (Ns/m)
12 Kf=500.9;        %Spring constant of floor (N/m)
13
14
15 a=Kf/Mf;
16 M1=(Mc+Mf)/(Mc*Mf);
17 M2=-1/Mf;
18 K1=Kg^2*Kt*Km/Rm/r_mp^2;
19 K2=Kg*Kt/Rm/r_mp;
20
21
22 %% STATE VARIABLE REPRESENTATION ——————————————————
23 % Input = Vm
24 % Neglect Jm & Beq
25 % Eff_m = Eff_g = 1
26
27 A=[0 0 1 0;0 0 0 1;0 a -M1*K1 0;0 -a K1/Mf -b/Mf]; %System matrix
28 B=[0;0;M1*K2;-K2/Mf];                              %Input matrix
29 C=[1 0 0 0;0 -a K1/Mf -b/Mf];                      %Output matrix
30 D=[0;-K2/Mf];                                      %Input-output
31                                                    %matrix
32
33 %% SIMULATED SYSTEM ——————————————————————————————
34
35 sys_Vm=ss(A,B,C,D);    %Steady state response
36
37
38 %% R: INPUT WEIGHT ——————————————————————————————
39 % Limitations: R>0, positive definite
40 % Large R: - Means u(t) must be small to keep performance index small
41 %          - Measns less control effort is used, which leads to
42 %                  -> Slower the poles
43 %                  -> Larger states
```

```
44
45 R=1;
46 % R=.1;
47 % R=.01;
48 % R=.001;
49
50
51 %% Q: OUTPUT WEIGHT ——————————————————————————
52 % Limitations: Q–NR^(−1)N'>0, positive semi−definite
53 % Large Q: − Means x(t) must be small to keep performance index small
54
55 %Start with Q=eye(4)
56 Q=eye(4);
57
58 %Increase values corresponding to the states you want to put more
59 %effort into keeping small.
60 % Q(2,2)=5;
61 % Q(2,2)=10;
62 % Q(2,2)=20;
63 % Q(2,2)=50;
64 Q(2,2)=100;
65
66
67 %% STATE FEEDBACK GAIN ——————————————————————
68
69 KL=lqr(A,B,Q,R)          %LQR feedback gain
70 AL=(A–B*KL);             %LQR system matrix
71
72 K=KL
73
74
75 %% SIMULATED SYSTEM ——————————————————————————
76
77 sys_L=ss(AL,B,C,D);
78
79 %% SIMULATION PLOTS ——————————————————————————
80
81 figure(1)
82 step(sys_L)
83
84 figure(2)
85 impulse(sys_L)
```

APPENDIX D
SIMULINK DIAGRAMS

D.1 State Observer
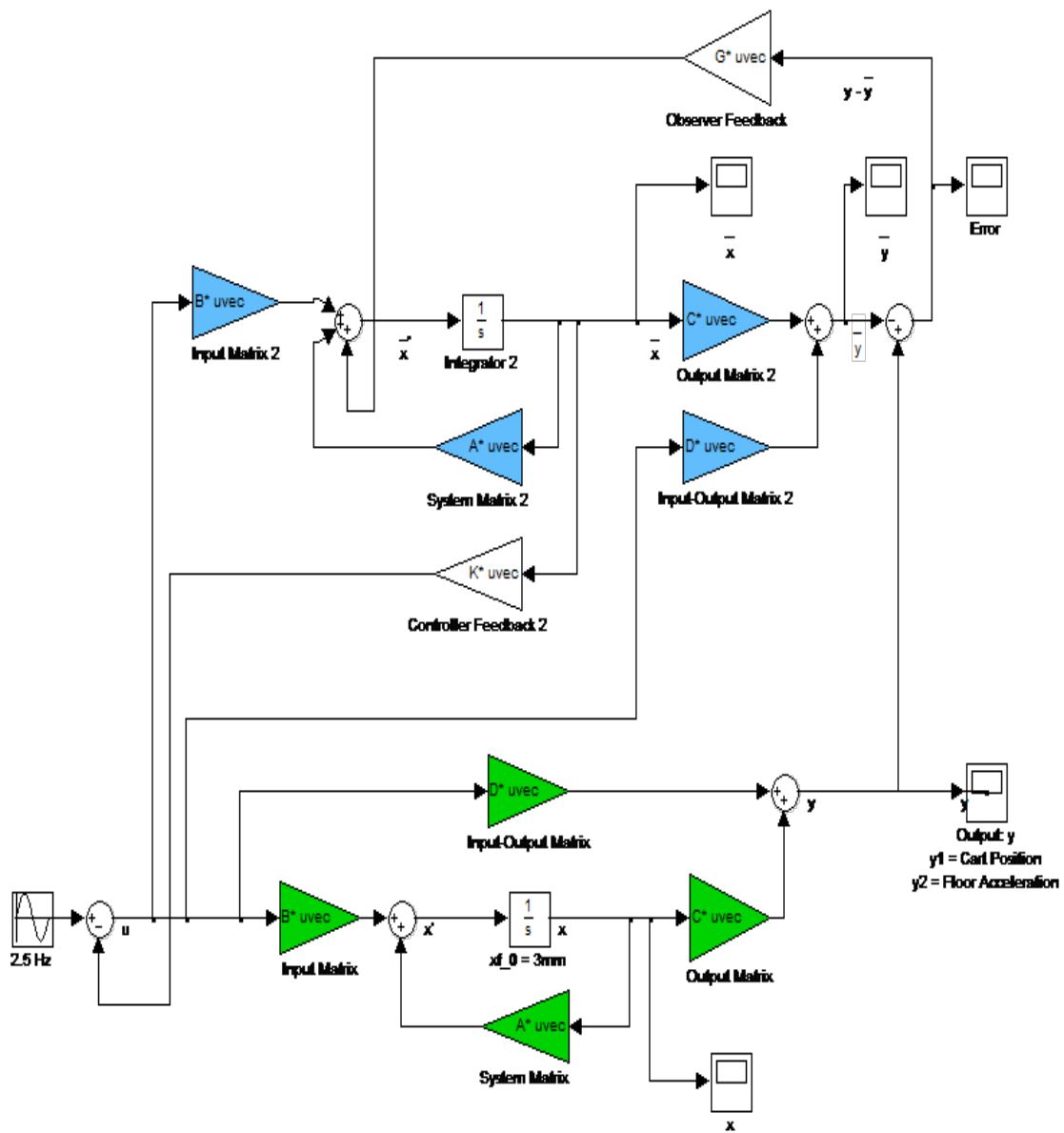
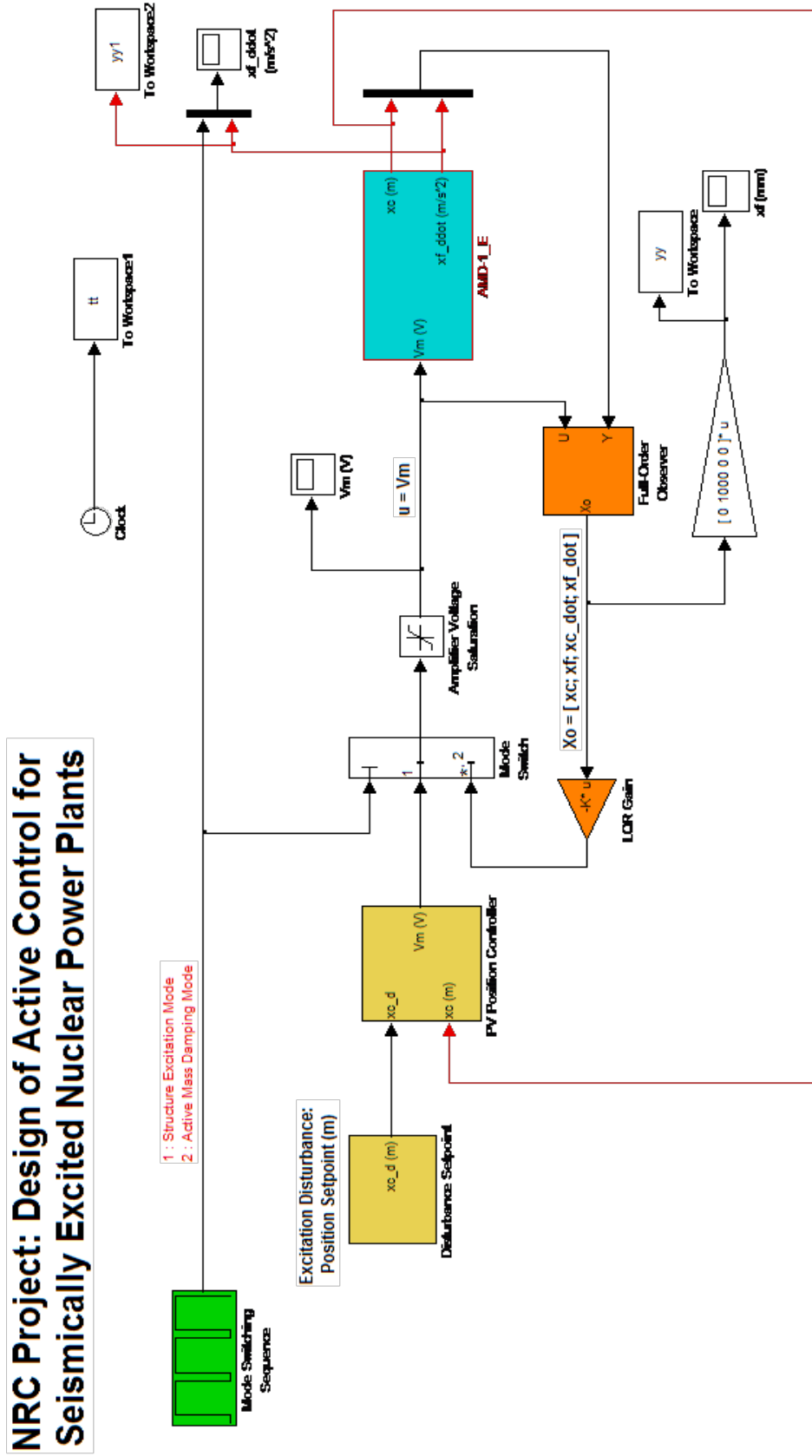FIGURE D.1: State observer Simulink diagram.

FIGURE D.2: Simulink model of the active control design for seismically excited Nuclear Power Plants [29].